INVITED REVIEW

This section of Journal of Materials Research is reserved for papers that are reviews of literature in a given area.

A review on low dimensional metal halides: Vapor phase epitaxy and physical properties

Yang Hu,[c] Yuwei Guo,[c] Yiping Wang, and Zhizhong Chen
Department of Materials Science and Engineering, Rensselaer Polytechnic Institute, Troy, New York 12180, USA

Xin Sun
Department of Physics, Rensselaer Polytechnic Institute, Troy, New York 12180, USA

Jing Feng
Faculty of Materials Science and Engineering, Kunming University of Science and Technology, Kunming City, Yunnan Province 650093, China

Toh-Ming Lu and Esther Wertz[a]
Department of Physics, Rensselaer Polytechnic Institute, Troy, New York 12180, USA

Jian Shi[b]
Department of Materials Science and Engineering, Rensselaer Polytechnic Institute, Troy, New York 12180, USA

(Received 3 April 2017; accepted 13 July 2017)

Excited by the great success of metal halide perovskites in the optoelectronic and electro-optic fields and the interesting emerging physics (Rashba splitting, quantum anomalous hall effect) of layered metal halides, metal halides have recently been attracting significant attentions from both research and industrial communities. It is shown that most progresses have been made when these materials are obtained at reduced dimensions. Among several growth methods, vapor phase epitaxy has been demonstrated with a universal control on morphology, phase, and composition. We thus believe that a thorough understanding on the physical properties and on the growth of general metal halide compounds at reduced dimensions would be very beneficial in the study of recent perovskites and layered metal halide materials. This review covers the physical properties of most studied metal halides and summarizes the vapor phase epitaxial growth knowledge collected in the past century. We hope that this comprehensive review could be helpful in designing new physical properties and in planning growth parameters for emerging metal halide crystals.

I. INTRODUCTION

In past several years, organic–inorganic perovskite metal halides have been exhibiting unprecedented successes in several technological fields. With the hybrid metal halide film as the solar absorber, the photovoltaic efficiency increased from around 3% to above 22% in less than six years.[1] At the same time, halide perovskite thin film-based high efficiency light emitting diodes[2] and photodetectors[3] have been demonstrated. Recently, optically pumped high quantum efficiency lasing[4] has also been achieved in low-dimensional halide perovskite crystals. These immediate successes of metal halide perovskites have been partially attributed to their exhilarating electro-optic and optoelectronic properties. As direct band gap semiconductors, they carry very high absorption coefficients and simultaneously have extremely long electron/hole lifetimes and diffusion lengths.[5–7] In the past several years, ferroelectricity[8,9] was discovered in several halide-based perovskites or perovskite structure-inspired compounds.

Along with the breakthroughs of metal halides in optoelectronics, recent studies have shown that metal halides could be promising materials in several other fields. Significant Rashba splitting[10–13] was recently proposed and revealed in several metal halide compounds, suggesting potential applications of these materials for novel spintronic logic and memory devices. More excitingly, recent explorations show that monolayer metal halide compounds may carry interesting ferromagnetic properties and even the quantum anomalous hall (QAH) effect.[14,15]

Fundamental studies have shown that the detailed crystal structure of the metal halides and also the related

Contributing Editor: Artur Braun
Address all correspondence to these authors.
[a]e-mail: wertze@rpi.edu
[b]e-mail: shij4@rpi.edu
[c]These authors contributed equally to this work.
DOI: 10.1557/jmr.2017.325

perovskite compounds play a critical role in enabling particularly interesting properties. With $CsPbI_3$ as an example, despite the same stoichiometric ratio, its high-temperature perovskite phase carries much more demanded optoelectronic properties than that of its low-temperature yellow phase[16] for photovoltaic applications. In addition, the composition of metal halides may also significantly influence the ultimate physical properties. For example, holding the same perovskite crystal structure, the organic–inorganic metal halide perovskite has been revealed to have a longer photoexcited electron/hole lifetime than that of its inorganic counterpart.[17] Finally, it is shown that most of these recent breakthroughs in metal halide materials have occurred when they are produced at reduced dimensions: thin films, monolayers, and nanostructures (e.g., two dimensional nanoflakes, one-dimensional nanowires and zero-dimensional quantum dots).

All these progresses from both scientific understanding and technological breakthroughs pose stringent requirements on material synthesis. Growth controls on crystal structure, composition, and crystal morphology are mostly demanded. Metal halides compounds carry a wide range of crystal structures as shown in Fig. 1: CsCl structure, fluorite, layered, zinc blende, wurtzite, rocksalt, and perovskite. Many different binary metal halide compounds can form very populous intermediate phases of ternary/quaternary compounds. Two examples[18,19] are given in Figs. 1(h) and 1(i). It is noted that when the crystal structures of two binary compounds are very different, the probability of forming intermediate phase compounds between them drastically reduces [Fig. 1(i)].

The complexity in the crystal structures and compositions of metal halides and the requirement on their morphology control down to monolayer suggest that vapor phase epitaxy may be one of the most effective approaches for materials synthesis. In vapor phase epitaxy, two key growth parameters, temperature and pressure, can be controlled in a very sophisticated manner so that the film quality and morphology can be designed down to the atomic scale. The high-temperature processing is generally applied during the vapor phase epitaxy, which helps reduce the defects such as grain boundary and metastable phases in as-grown metal halide materials. Epitaxy can stabilize certain demanded crystal structures; a variety of vapor deposition growth methods, such as molecular beam epitaxy (MBE), sputtering, chemical vapor deposition (CVD), and physical vapor deposition (PVD) can be chosen to manipulate growth parameters to precisely control material compositions.

Motivated by these, in this review, we will cover two major aspects of metal halide materials: physical properties and vapor phase epitaxy. It is noted that there are many great review articles on the topic of optoelectronic/electro-optic properties of metal halide perovskites, but there is a vacuum on the comprehensive review of the

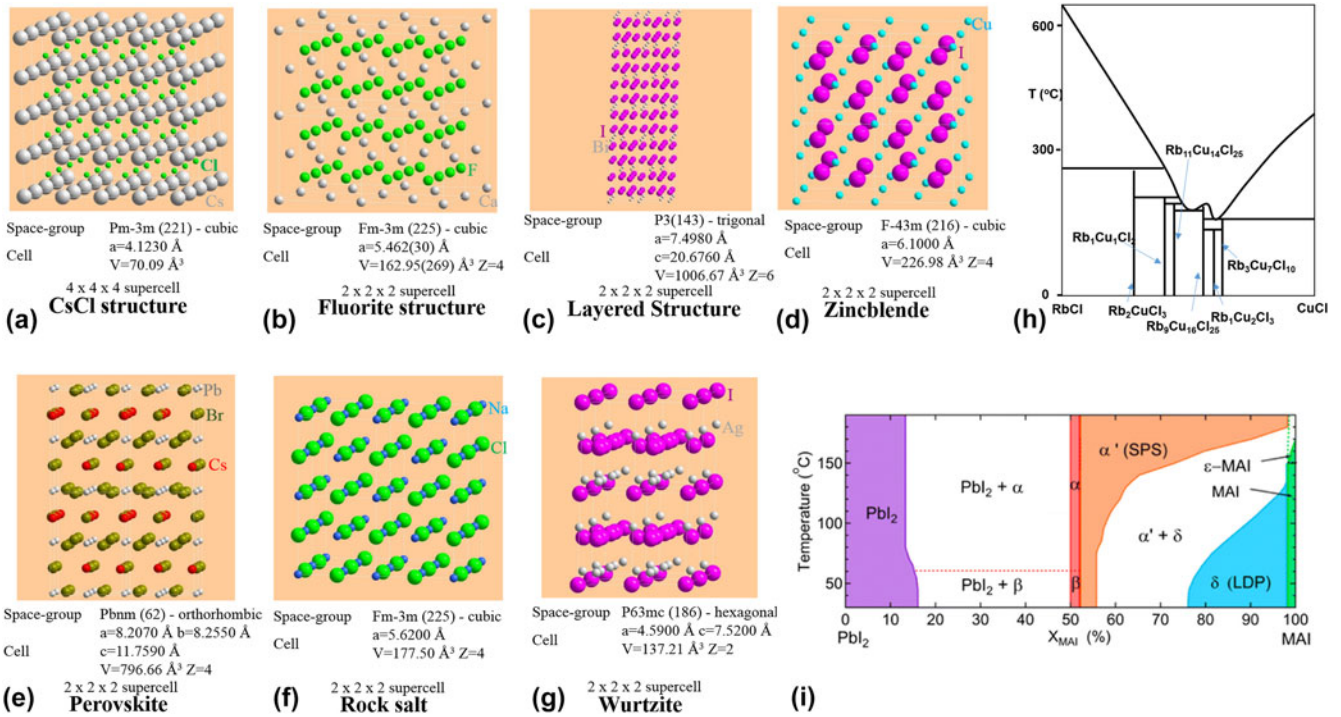

FIG. 1. (a–g) Crystal structures of metal halides; (h, i) two examples of phase diagrams of metal halides. Reproduced with permission from Refs. 18 and 19.

interesting properties in general metal halide compounds. It is also noted that, it is the right time to assemble the most significant progresses on the vapor phase epitaxy of metal halides. Plenty of knowledge has been collected in the past several decades on this field. A timely review on this topic will help us better understand the growth kinetics and develop effective growth strategies especially for the recent metal halide perovskites and layered metal halides with promising applications in electro-optics, optoelectronics, and spintronics.

II. PHYSICAL PROPERTIES

Ionic bonds and van der Waals bonds are two typical bonding types found in most metal halide compounds. It has been found that the bonding energy of most ionic bonds in metal halides is relatively small. Correspondingly, many metal halides are very sensitive to external stimuli such as photon illumination, electron beam, radiation, chemicals, electric field, temperature, and pressure. The ultrasensitive character of metal halides to environmental perturbations, the extreme ionicity of their bonding nature, and the small bonding energy endow them with many interesting physical properties such as photodecomposition, electron beam-induced decomposition, low-density deep level defect states/high photon-electron conversion efficiency, chemically induced electrical conductivity modifications, ferroelectricity and so on. This section broadly summarizes the major physical properties in nonperovskite metal halides that people have discovered in the past several decades. We hope the review on these progresses in nonperovskite metal halides could help researchers gain a more fundamental understanding in researching perovskite metal halides and inspire new discoveries in more general metal halide compounds.

A. Photodecomposition

The relatively low decomposition temperature of metal halides makes them very vulnerable under photon irradiation. In 1893, Wells[20] first observed $PbBr_2$ turning to black upon exposure to sunlight. Two years later in 1895, Norris confirmed that black color was due to the formation of lead during irradiation and that bromine was lost during the process as well. In 1923, Sanyal et al. also reported bromine loss upon radiation. In 1964, 1965, Tubbs's group[20–22] studied the photodecomposition of PbI_2 in air or vacuum with the forms of single-crystal, polycrystalline, and evaporated film samples. Photolysis process led to the release of iodine and to the formation of lead. The decomposition rate followed the intrinsic absorption spectrum of PbI_2, and the onset wave length was found to be at 530 nm. The photodecomposition of PbI_2 was revealed not to occur at room temperature but increased exponentially with the temperature from 393 to 493 K. This was the first halide layer demonstrated to have high-resolution image recording applications. In 1966, Kaldor and Somorjai[23] first studied $PbCl_2$ using opaque layers with a thickness of 20 μm which were prepared by vacuum evaporation. Thermal decomposition of $PbCl_2$ occurred above 473 K, and photodecomposition occurred above 298 K. Chlorine was released, leaving behind a dark gray lead precipitate after decomposition. The minimum photon energy required to initiate photodecomposition was found slightly lesser than that of the absorption edge. It was probably due to the electron transition from the valence band to the $PbCl^+$ cation whose energy state is located at about 0.7 eV below the conduction band. In 1967, Spencer and Darlak[24] studied microcrystalline $PbBr_2$ dispersions which had a large surface-to-volume ratio. The dispersions of $PbBr_2$ in polyvinyl alcohol–water solution were prepared at room temperature by simultaneously pipetting 25 mL $Pb(NO_3)_2$ and 25 mL KBr into 50 mL 0.5 wt% polyvinyl alcohol–water solution. Needle-like $PbBr_2$ microcrystals were obtained which were several tens of microns long and shorter than one micron along radial directions. The photodecomposition rate was measured as the rate of lead production under an ultra-violet irradiation at 295 K. A linear relation between the lead production rate and intensity of irradiation was revealed.

In 1960, photodecomposition of CdI_2 was observed by Fotland.[25] The sample was prepared by soaking filter papers into a concentrated CdI_2 solution and then dried in air. Then the filter paper was exposed to a 100 W mercury arc lamp for 15 s. It was observed that the filter paper turned dark brown. The color change was due to the production of small cadmium particles near the surface upon photodecomposition. The sensitivity of CdI_2 was determined by its intrinsic absorption spectrum. The sensitivity became significant with the wave length of light shorter than 410 nm. With its good resolution and high sensitivity, CdI_2 print-out papers were widely used for recording ultra-violet light spots from galvanometer oscillographs and for preparation of light-sensitive electrophotographic materials. For instance, cadmium halides or lead halides were often added to silver halide–copper halides mixtures to further improve contrast or speed.

In addition to lead halides and cadmium halides, other halides with photodecomposition properties were also revealed: $BiCl_3$, BiI_3, SbI_3, AgBr, and AgCl.[26–33] The photolysis of these compounds was found to be useful in studying reaction kinetics and for imaging applications. However, the photolysis property should be carefully considered in characterizing the optoelectronic properties of these materials, especially at a low dimension. In addition, the fundamental understanding received in studying the photodecomposition of binary metal halides could be applied to investigate the photo-induced phenomena in metal halide perovskites.

B. Electron-induced decomposition

Besides photo-induced decomposition, as expected, people discovered that these metal halide compounds could be decomposed and evaporated under electron beams. In 1984, Muray et al.[34] used e-beam Ultra High Vacuum evaporation to prepare an 80 nm thick AlF_3 amorphous film with high uniformity on thin carbon films and on 50-nm-thick Si_3N_4 windows. AlF_3 can act as an e-beam resist,[35] which enables precise linewidth controllable lithography. AlF_3 is a selfdeveloping resist, which volatilizes during exposure to radiation. To volatilize the AlF_3 film to create patterns, the incident electron beam had an energy of 100 keV, a beam current of 10^{-11} A, and a spot size of 0.5 nm. Under such experimental conditions, it was found that a dose of 10 C/cm^2 was sufficient to result in a total mass loss in the 80-nm-thick AlF_3 film. Such a high-resolution resist enables replication of nanoscale patterns, down to several nanometers, onto Si_3N_4 and many other substrates. AlF_3 film demonstrated a promising application as a resist for electron beam lithography, however, its requirement of an extremely high current density to vaporize the metal component limit is of practical use in device fabrication.

In 1992, Langheinrich et al.,[36] used an electron gun evaporator to evaporate LiF and AlF_3 powders in a weight ratio of 10:1 onto a liquid nitrogen-cooled substrate holder at about 90 K. The substrate was Si_3N_4 or thin carbon foil. Both the low-substrate temperature and a mixture of the two components with different structures prohibited the formation of crystals, resulting in a homogeneous and quasiamorphous AlF_3-doped LiF film with high resolution and sensitivity. This LiF-based film can be effectively be evaporated under an electron beam energy of 100 keV and a beam current between 100 and 300 pA. The critical exposure was linearly related to the film thickness. The dose condition for this study was much less than that of the pure AlF_3 case. Both the high resolution (below 7 nm) and high sensitivity of the AlF_3-doped LiF film demonstrate a great capability of being a practical resist in device fabrication.

In addition to AlF_3 and LiF, researchers[37,38] also explored various metal fluorides as a positive and negative photoresist. A 50 nm thick FeF_2 film was vacuum deposited and had a polycrystalline structure. When used as a positive resist, matrix dots of 4 nm in diameter were obtained under exposure conditions of 10 pC per dot exposure at 100 keV. Under high doses, a high amount of intrinsic stress was found to build up in parts of the film adjacent to positive exposures due to the loss of fluorine. When FeF_2 was used as a negative resist, it was exposed at 20 keV and 250 nC/cm and then developed in water. Polycrystalline films of BaF_2 and SrF_2, typically 40 nm thick, were not suitable for positive resists, but their negative resists were developed. They were exposed to 20 keV electrons with a line dose of 100 nC/cm and then were developed in water since they were soluble in water. A 50 nm thick amorphous thin film of CrF_2 resembles the structure and exposure properties of AlF_3. When used as a positive resist at 20–50 μC/cm and 100 keV, clear patterns can be observed on the resist after selfdeveloping. However, the pattern cannot be transferred to a substrate because ion etching was inhibited by the leftover of a thin layer of Cr on the substrate after selfdevelopment. CsF formed islands, instead of continuous films on the substrate. It was used as a positive resist and exposed under 100 keV and 0.5 μC/cm. The line dose applied to CsF was very small because it had a very high sensitivity, almost two orders higher in magnitude than that of the AlF_3 film of comparable thickness. Pattern characters of size 40 × 40 nm could be resolved.

C. Optoelectronic/electro-optic properties

Most metal halides are either semiconductors or insulators with a significant portion of them carrying band gaps at the UV regime. For a long time, people have been interested in exploring metal halides for optoelectronics and electro-optics. Though many heavy metal halide materials were used as radiation detection materials or as scintillating materials, wide interests in applying metal halides for much broader applications, such as solar cells, photodetectors, optically pumped lasing, and light emitting diodes have only emerged recently.

In 1961, Kuwabara and Aoyagi[39] studied the photoconductivity of KI, KBr, and KCl in the fundamental absorption range between 203 and 383 K. A vacuum monochrometer was used to measure photocurrents of the crystal pressed between two electrodes. The light intensity during the experiment was kept constant at 10^{10} photons/cm^2. Three characteristic regions were identified in their spectral: a bell-shaped peak in the low energy range due to impurities; a faint photoconductivity at the first absorption peak; and a photoconductivity arising from direct photoionization, which is temperature independent. Direct photoionization refers to that, free carriers are directly created by incident photons with energies larger than the ionization energy. The ionization in this spectra range occurs with almost a constant quantum efficiency independent of the photon energy or temperature.

Evans[40] showed that SbI_3 could be prepared by melting the mixture of pure antimony and iodine in a stoichiometric ratio in an evacuated silica tube. These crystals had their optical axis (*c*-axis) perpendicular to the crystal plate. Photoconductivity of SbI_3 was conducted at room temperature on a Perspex aperture and was in contact with two spring-loaded platinum electrodes separated by 0.7 mm. In dark, the resistivity of SbI_3 at room temperature was 10^9 Ohm cm. Photoconductivity was

measured at various wave lengths of incident light while keeping the intensity, exposure time, and area constant. The potential difference between the electrodes was 20 V. The photocurrent reached two maxima at wavelengths of 580 and 440 nm. The current peak at 580 nm was due to an increasing rate of carrier recombinations as the absorption coefficient increases near the band gap, and the peak at 440 nm was contributed by a similar mechanism associated with exciton states of high energy.

Lefkowitz et al.[41] applied a new technology to prepare thin single crystals of thallium halide. The TlBr crystals were obtained by thin sectioning a parent crystal with a modified ultramicrotome at room temperature while TlCl crystals were sectioned at about 373 K. The ability to obtain good single crystals enables further optical characterization of the materials. The absorption spectra of TlBr and TlCl were measured at 4 K. Two new exciton states for the (100) plane of TlBr were found at 401 and 399 nm. A band gap of 3.115 eV at Γ point was confirmed. The analysis on the absorption spectrum of TlCl showed two lines at $n = 1$ state, indicating a spin orbit splitting of the valence band. In 1967, Baldini and Bosacchi[42] widely studied optical properties of alkali-halide crystals. They applied reflectivity measurements to single crystals of alkali halides in the ultraviolet region of the spectrum, in which excitonic and low interband transitions occurred. Based on both calculation results and their observation during experiments, they were able to predict properties of band structures of alkali halides, describe low-lying excited states, and establish a relation among energy levels of the conduction band, L bands, and the F center.

In 1977, Olive Less Hsu and Clayton Bates, Jr.[43] used a nonionizing light source to obtain excitation and emission spectra of well-annealed zone-refined CsI (Na) specimens in the temperature range from 300 to 4.2 K. Nonionizing light refers to the photon energy that is lower than the energy required to ionize atoms or molecules, that is, kicking off electrons above the vacuum level. Nonionizing light can have energy either higher or lower than the band gap energy. Two kinds of emissions were observed. One is the characteristic blue emission and others are low-temperature emissions. For the first time, they discovered that the characteristic emission consisted of two bands at 420 nm and 370 nm, respectively. Compared with calculated localized exciton energies, they concluded that the characteristic emission is due to the radioactive recombination of relaxed sodium impurity excitons. This study demonstrated the significance of excitation spectra in understanding the luminescence phenomenon of materials.

In 2002, Larruquert et al.[44] explored optical properties of evaporation-deposited thin films of CsI, KI, and KBr and their quantum efficiencies in the 53.6–174.4 nm spectral range. The optical constants were obtained from reflectance measurements. Effects of film heating and UV irradiation on the films' optical properties and quantum efficiency were also investigated. The maximum absolute quantum efficiencies for as-deposited CsI, KI, and KBr were experimentally measured to be 0.85 at 105 nm, 0.78 at 52 nm, and 0.68 at 62 nm, respectively. It was found that KBr tended to have the highest stability upon thermal treatment and UV irradiation. KI film's optical properties were clearly affected by UV exposure but were relatively intact upon heating. Both optical properties and the quantum efficiency of CsI were changed under conditions of heating or UV exposure. Correlations between the change in optical constants and the change in quantum efficiency were also determined.

In addition to binary metal halides,[45–48] the study on the optoelectronic/electro-optic properties of the ternary metal halides was scarce before 1990. Very recently significant progress on understanding and revealing the optoelectronic/electro-optic properties of halide perovskites was made along with the technological breakthrough in their solar applications. One of the most significant discoveries[6] was that a direct band gap semiconductor $CH_3NH_3PbI_3$, at its thin film form, and the photoluminescence-based electron hole carrier lifetime could reach a few hundred nanoseconds and the electron/hole diffusion length exceeds one micrometer (Fig. 2). The high quantum efficiency of the ternary compounds led to a recent demonstration of optically pumped lasing[4]

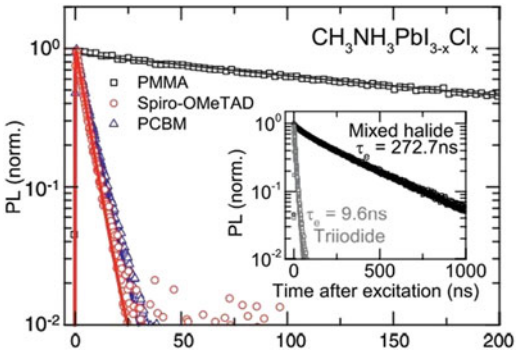

FIG. 2. Time-resolved PL of metal halide perovskite thin films. Reproduced with permission from Ref. 6.

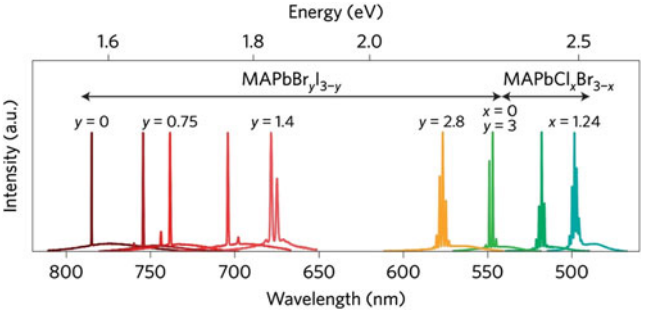

FIG. 3. Lasing of metal halide perovskite nanowires. Reproduced with permission from Ref. 4.

(Fig. 3). Due to the focus of the current review, for more studies on the optoelectronic properties associated with metal halide perovskites, the readers are recommended to refer to related review articles such as.[1]

D. Magnetic properties

Serious studies on the magnetic properties of metal halides date back to several decades ago. In 1965, Dillon et al.[49] studied magneto-optical properties of ferromagnetic chromium trihalides. The experimental investigations showed that the very large specific magnetic rotations were related to the absorption band edges of $CrBr_3$ and $CrCl_3$. Comparison with theoretical results enabled the attribution of the absorption band edge to the electron transfer transition between two orbitals. The large rotations which resulted from energy level splitting were due to spin–orbit interactions of the final state and the trigonal crystal field. In 2017, Xu et al.[14] demonstrated ferromagnetism in atomically-thin CrI_3 flakes (Fig. 4). The CrI_3 flakes were obtained by the mechanical exfoliation of bulk crystals and were then transferred to oxidized silicon substrates. The process was operated in a glove box under inert atmosphere. CrI_3 flakes with a different number of layers were obtained with thickness of about 0.7 nm/layer. The layered structure enabled the study of thickness-dependent magnetism and the coupling between the underlying substrate and thin film if the interaction strength is strong. Magneto-optic Kerr effect measurements as a function of the applied external magnetic field were applied to probe the magnetic order of CrI_3. The observed hysteresis loop and remnant magnetism at the zero external magnetic field confirmed the ferromagnetic ordering of CrI_3 layers. Ferromagnetism of CrI_3 varied with layer thickness, which was confirmed by their different hysteresis loops and remnant/saturation Kerr rotation values. The intrinsic ferromagnetism in monolayer CrI_3 and its layer-dependent magnetic response revealed promising applications in investigating the emerging quantum effect in hybrid structures and in developing novel magneto-optoelectronic devices.

Kyungsoo Ahn et al.[50] used powder neutron diffraction on the triangular-layer system $Tb_2C_2I_2$ to investigate the effects of geometrical frustration on its magnetic properties. Below 60 K, strong resolution-limited magnetic Bragg reflections were observed due to commensurate antiferromagnetic long range (afm) ordering. Above this, the commensurate afm transition at 60 K and the magnetic behavior of $Tb_2C_2I_2$ can be divided into three regions. Below 150 K, increased afm short-range correlations developed within the Tb atom double layers. Interplane correlations kicked in when the temperature was below 95 K. The interplane correlations remained short ranged at about 1 nm. Sizable interplane correlations started to develop when the temperature was reduced close to 87 K. These sizable interplane correlations were raised from extended intraplane correlations, which grew rapidly in a sharp temperature range around 87 K. The discontinuous transition of interplane correlations growth resulted in the transition from the commensurate phase to the incommensurate phase due to the magnetic fluctuation of Tb moments as the temperature increased above 87 K.

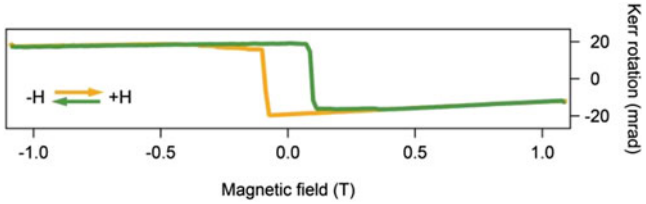

FIG. 4. Magnetic properties of monolayer CrI_3. Reproduced with permission from Ref. 14.

Kasten et al.[51] explored the magnetic ordering in GdI_2. The GdI_2 powder samples were prepared from a solid state reaction between GdI_3 and metallic Gd. The powder samples were composed of tiny platelet-shaped crystals in a hexagonal structure with the *c*-axis perpendicular to the plane. The GdI_2 crystal possessed a strongly two-dimensional structure with Gd layers separated by two I layers along the hexagonal *c*-axis. AC susceptibility measurements were performed on the sample with changing temperature. It was observed that under about 290 K, GdI_2 had a very high temperature-independent susceptibility under a zero external magnetic field. As temperature increased higher than 290 K, there was a sharp decrease of susceptibility at around 295 K due to metallic Gd impurities. Above the material's Curie temperature, T_C = 313 K, the susceptibility remained almost constant up to 400 K, so no Curie–Weiss behavior was observed in this temperature range. Effects of small external magnetic fields (<0.03 T) on susceptibility were also investigated. It was found that above T_C, the external magnetic fields had no influence on the susceptibility while below T_C, the susceptibility dropped dramatically upon the application of a static magnetic field and was reduced to the susceptibility value above T_C within a few mT and stayed constant with the further increased magnetic field. The analysis of the crystal structure and ground spin state of ions revealed a two-dimensional magnetic interaction with superexchange via conduction band electrons within one layer. The large-high temperature susceptibility compared to metallic Gd indicated that the dominant magnetic ordering is a ferromagnetic interaction. Besides, the absence of the Curie–Weiss behavior can be explained by two-dimensionality of the Heisenberg interaction. On the other hand, the low-temperature experiments confirmed the antiferromagnetic intersublattice coupling. This ideal Heisenberg, two-dimensional system is very appealing for both experimental and theoretical studies.

Recently, Huang et al.[15] used first principle calculations to theoretically predict the QAH effect in the ferromagnetic transition metal halide RuI_3 monolayer. The RuI_3 monolayer was predicted to be an intrinsic ferromagnetic QAH insulator with a topologically nontrivial band gap of 11 meV at the Fermi level attributed to its crystal symmetry. As a consequence, the QAH effect of RuI_3 was expected to be robust. Strain engineering was also proposed by the authors to be a possible method to manipulate the crystal's exchange energy and band gap. The robust QAH effect in RuI_3 showed promising applications in nanoelectronics and spintronics. These recent experimental and theoretical progresses in exploring the magnetic properties of low-dimensional metal halides may inspire exciting discoveries in halide systems.[11,52,53]

E. Chemical-induced electrical conductivity modification

The ionic nature of metal halides makes these materials sensitive to certain gases. In 1999, Lauque et al. invested the sensor characteristics for the NH_3 gas of CuBr films.[54] The CuBr film was prepared by Radio Frequency Sputtering (RF sputtering) on the epoxy substrate. The RF power used in the experiment was 50 W, the targets are CuBr targets formed by pure CuBr powder, and the sputtering was conducted under an argon pressure of 3 Pa. The substrate was kept at room temperature during sputtering. The as-deposited film showed a randomly orientated polycrystalline γ-CuBr structure confirmed by X-ray diffraction. To investigate the film's electrical conductivity in the presence of ammonia gas, the film on the epoxy substrate was then combined with interdigital copper electrodes. It was shown that the DC conductivity of CuBr film reduced upon increasing partial pressure of NH_3. The electrical response was also very fast, in the order of a few seconds. The reduction in DC conductivity was believed to be caused by strong interactions at the gas–solid interface between CuBr and NH_3. This interaction resulted in formation of surface copper ions and these positive surface charges were balanced by an adjacent space charge region enriched in copper vacancies and electrons. The increased electron concentration decreased the original p-type conductivity of the film. Besides, the adsorbed NH_3 gas on the film surface increased the interfacial resistance and further reduced its DC conductivity. The sputtered CuBr film demonstrated a promising application as a faster response sensor for NH_3. In 2004, the same group, Lauque[55] developed high sensitivity and selective room temperature NH_3 gas microsensors based on a CuBr film. In the presence of ammonia, the reaction between ammonia molecules and copper ions on the film surface result in a large decrease in the film conductivity, which can be used as a sensing signal. The operation ammonia concentration is between 1 and 500 ppm. Its high sensitivity, selectivity, and ability to operate at room temperature provides itself with great practical application possibilities.

Besides CuBr, a similar sensing behavior occurs in AgCl. In 1990, Lauer, Maier, and Gopel[56] investigated conductance effects of ammonia on different types of AgCl films. The three kinds of films were epitaxial: AgCl film on the (100) NaCl substrate, polycrystalline AgCl film on sapphire, and freestanding AgCl film. The epitaxial (100) AgCl films were prepared by evaporating pure AgCl onto NaCl single crystals with thickness of 150, 200, and 300 nm. The polycrystalline films with thickness of 100 nm were obtained also by evaporation onto a sapphire substrate. Annealing was necessary for both films in contact with a substrate to achieve equilibrium conductivity. The freestanding films with thickness of 190–200 nm were prepared by the precipitation of AgCl from $AgNO_3$ and HCl under protective light. The film conductivity measurements were carried out with an impedance bridge in the temperature range of 373–443 K and an ammonia partial pressure range of 10^3–10^5 Pa. The conductivity of the AgCl film was determined by two competing factors. First, the AgCl is p-doped by Ag^+ vacancies. So, an increased concentration of Ag^+ vacancies enhances the film's conductivity. Thus, with the presence of ionophilic NH_3 gas, the Ag^+ cations combined with the NH_3 molecule to form complexes that increased Ag^+ vacancies, which resulted in an increase of conductivity. Second, the adsorption layer of gas such as NH_3 results in interfacial transfer resistivity, reducing the film conductivity. Thus, upon the presence of NH_3 gas, the conductivity of the AgCl film decreased and the response time was usually 1–5 min in the temperature range of 373–973 K, revealing a possible application in the gas sensing field. In addition to NH_3, several other gases such as CO_2 sensing[57–65] were also practiced.

F. Ionic conductivity

The low decomposition temperature of metal halides suggests that the defect formation energies in these materials are relatively small compared to those of oxides dielectrics. Both low decomposition/melting temperatures and low-defect formation energies may make these materials interesting for battery-based applications concerning ionic conductivity. In 1986, Coetzer[66] reported the first disclosure of a high energy density system that used transition metal chlorides as a solid cathode. Solid electrolyte β-alumina was used as a separator. The second electrolyte, molten $NaAlCl_4$, was incorporated with the cathode, and the electrochemically active species in cathode was insoluble in this

molten salt electrolyte. This second liquid electrolyte served to transport sodium ions between β-alumina and the reaction zone in the cathode. This battery set-up had low cost and high safety reliability, possessing great potential for a wide range of commercial applications, such as vehicle traction, load leveling, and aerospace applications.

Another example is associated with sodium/nickel chloride battery. In 2001, Sudworth[67] explored the operating principle, performance, production and applications of sodium/nickel chloride battery. The sodium/nickel chloride cell is composed of molten sodium as the negative electrode, nickel or nickel chloride as the positive electrode during discharging or charging processes, respectively, and molten sodium tetrachloroaluminate (liquid) and β-alumina (solid) as the electrolyte. The liquid component of the electrolyte promoted the rapid transport of sodium ions between the nickel chloride electrode and the solid ceramic electrolyte. The minimum operating temperature of the cell is determined by the melting temperature of its electrolyte, 430 K, but the optimal temperature range for the best battery performance was found to be between 543 and 623 K. The performance of cells was found to be optimal under a current limit of 15 A per cell for a 32 A h cell and with a charging voltage of 2.67 V. The sodium/nickel chloride battery could be used in both pure electric and hybrid vehicles, telecommunications, and marine applications. In addition, there are several other examples that take advantage of the ionic character of metal halide films for battery applications.[68–86]

G. Radiation-induced electrical conductivity modification

The semiconducting nature and the involvement of heavy elements of metal halides make them ideal for radiation detection. In 1948, Hofstadter[87,88] reported the discovery of scintillator NaI mixed with a small amount of thallium. The sample was prepared in vacuum in a 0.5-inch quartz tube. Its radiation detection capability was tested by exposure to a source of 0.1 mCi radium at 16 cm at room temperature. The response of the sample was characterized by light flashes emitting in about one microsecond or less, indicating a quick response as a detection material. This discovery revolutionized the field of radiation detectors.

In 1970, Roth and Willig[89] studied PbI_2 as nuclear particle detectors. The PbI_2 detector was made from platelets of vapor-grown single crystals with 1 cm diameter. The front contact of the gold layer was deposited by evaporation and was connected to a copper wire by a silver paste. The rear contact used a silver paste film. The pulse height was measured, which is proportional to the number of collected charge carriers created from particle radiation. Both α and γ particles were counted in the temperature range from 73 to 403 K. The operation temperature range of PbI_2 was larger than that of other semiconductor detectors such as CdTe, Si, and Ge. It also had better γ-ray absorption properties. The reports demonstrated a promising application of PbI_2 as an accurate radiation detector with a wider operation temperature range.

van Loef et al.[88,90] used optical, X-ray, and γ-ray excitations to study scintillation properties of $LaCl_3$ doped with different concentrations of Ce^{3+}. It was found that the activator, Ce^{3+} ion had emission peaks at 330 and 352 nm under optical and γ-ray excitation. The samples with Ce^{3+} concentration varying from 2% to 30 and 100% had photon yields of 46,000 ± 3000 photons per MeV of absorbed γ-ray energy. It was also found that the short decay component of the total light yield in the scintillation decay curve increased with the Ce^{3+} concentration. The energy resolution was measured and the highest resolution of about 3.1% was given by the sample with 10% Ce^{3+}. Ce^{3+} activated $LaCl_3$ had been demonstrated to be faster and more efficient for high-energy resolution scintillation.

$LaBr_3$ was studied as a scintillating material intensively.[88,91,92] Recently, Shah et al. studied the Ce^{3+} doped $LaBr_3$ scintillator for γ-ray spectroscopy. The crystals were prepared using the Bridgeman method. The molar concentration of Ce^{3+} in $LaBr_3$ crystals was 0.5%. Under gamma ray excitation, the Ce^{3+} emission peaked at 360 nm. The sample had a large light output larger than 60,000 photons/MeV and a fast principle decay constant smaller than 30 ns. The energy resolution was about 2.6% for the 662 keV full absorption peak. A study conducted by van Loef et al. on 0.5% Ce^{3+} doped $LaBr_3$ showed similar properties under γ-ray excitation. These research results confirmed that $LaBr_3$–Ce could be one of the ultimate choices for a scintillator, especially in the case where good energy resolution and fast luminescence decay are required.

Heavy metal halide LuI_3 was also explored for radiation detection.[88,93] In 2006, Birowosuto et al. investigated the scintillation properties of Ce^{3+} activated LuI_3. Single crystals of Ce^{3+} doped LuI_3 were prepared by the Bridgmann technique. γ-ray pulse height spectra of samples were recorded. An extremely high light output of 92,000 $e–h^+$ pairs/MeV was observed for LuI_3: 5% Ce^{3+}. The best energy resolution of 3.3% at 278 K was obtained in the sample with 0.5% Ce^{3+} and a light output of 50,000 $e^––h^+$ pairs/MeV. The γ-scintillation decay spectra presented that about 50% of the total light yield was produced within 50 nm. Its very high light output, acceptable energy resolution, and reasonable high density made itself a material of interest in this field.

H. Superconductivity

Encouraged by the great success of high-temperature oxide superconductors with layered structures, different layered metal halide materials[94–98] have been proposed and studied in the search of high T_C superconductors. In 1996, Henn et al.[99] applied resistivity, susceptibility, and specific heat measurements to characterize the superconducting state of layered superconductors $Y_2C_2I_2$ and $Y_2C_2Br_2$. Single phase samples of $Y_2C_2X_2$ (X = Br, I) were prepared by heating a mixture of Y metal chips, YX_3, and graphite powders in sealed tantalum crucibles at 1320 Both electrical resistance measurements from 300 to 4 K and susceptibility measurements in an external field of 1 mT from 2 to 15 K were conducted. The sudden vanishing of electrical resistivities were observed at 5.0 and 10.0 K for $Y_2C_2Br_2$ and $Y_2C_2I_2$, respectively. Besides, the dramatic decrease of magnetic susceptibilities occurred at 5.04 and 9.97 K for $Y_2C_2Br_2$ and $Y_2C_2I_2$, respectively. These results from two measurements agreed well with each other, so the superconductivity temperature was confirmed to be 9.97 K for $Y_2C_2I_2$ and 5.04 K for $Y_2C_2Br_2$. The heat capacities obtained from the two compounds were in excellent consistence with the two-fluid model, indicating a moderately strong electron-phonon coupling which increased the transition temperature.

In 1996, Shoji Yamanaka et al.[100] discovered a new layer-structure nitride, β-ZrNCl displaying superconducting property upon intercalation with lithium. The β-ZrNCl crysral is formed by sandwiching ZrN double layers between two close packed chloride layers, represented as [Cl–Zr–N]–[N–Zr–Cl]. It was confirmed by XRD that the crystal possessed a rhombohedral unit cell with three layers. The β-ZrNCl crystals were prepared by reaction of ZrH_2 and NH_4Cl at 650 °C. The lithium intercalation was conducted by dispersing β-ZrNCl into 15% *n*-butyllithium (Bu-Li) solution. The final product obtained had the formula of Li_xZrNCl with $x = 0.16$. Both magnetic susceptibility under field intensity of 50 Oe and electrical resistivity of Li_xZrNCl were measured with changing temperature. These two measurements reveal a superconducting transition temperature of 12.5 K. Besides the observed hysteresis loop, magnetization measurement indicated that the lithium intercalated β-ZrNCl is a type-II superconductor. Later in 1998, Yamanaka et al. showed this material exhibited a superconducting state with a high Curie temperature of 25.5 K with processing optimization.[101]

Very recently, Yin and Kotliar[102] proposed a design guideline to prepare mixed-valent high-T_C superconductors. They used first-principles calculations and focused on increasing Curie temperature of thallium halide-based compounds, in which superconducting state arises due to a strong electron-phonon coupling. Superconducting properties of $CsTlF_3$ and $CsTlCl_3$ were studied with various hole doping levels and volumes and the Curie temperatures were predicted to be 30 and 20 K with ~0.35/f.u. hole doping at modest pressures, ~10 and ~2 GPa, respectively.

I. Rashba splitting

Rashba splitting as a consequence of strong spin-orbital interactions and a lack of inversion symmetry, suggesting promising applications in the field of logic computation and memory (e.g., spintronics), has been discovered in several halide materials.[10,12,103–109] In 2011, Ishizaka et al.[13] discovered a giant Rashba-type spin splitting in bulk BiTeI (Fig. 5). The single crystals of BiTeI were prepared by the Bridgeman method. It was confirmed that there existed a huge spin–orbit interaction in the polar semiconductor BiTeI, which contains heavy elements. Due to this strong spin–orbit interaction, bulk carriers were ruled by the Rashba effect, which lifted the electron-spin degeneracy, resulting in spin splitting. The observed band splitting and spin polarization were consistent with first-principles calculation. In 2013, Landolt et al.[110] applied angle-resolved photoemission spectroscopy (ARPES) in the ultra-violet and soft X-ray regime to explore the giant Rashba spin splitting in the bulk conduction and valence bands of BiTeCl. ARPES enabled separation of bulk and surface contribution of the electronic structure and revealed that the Te-terminated (0001) crystal surface had spin-split two-dimensional surface states. A large Rashba splitting of both the bulk and surface states of BiTeCl was observed. Together with its large band gap and macroscopic crystallinity, it became an interesting material for spin transport

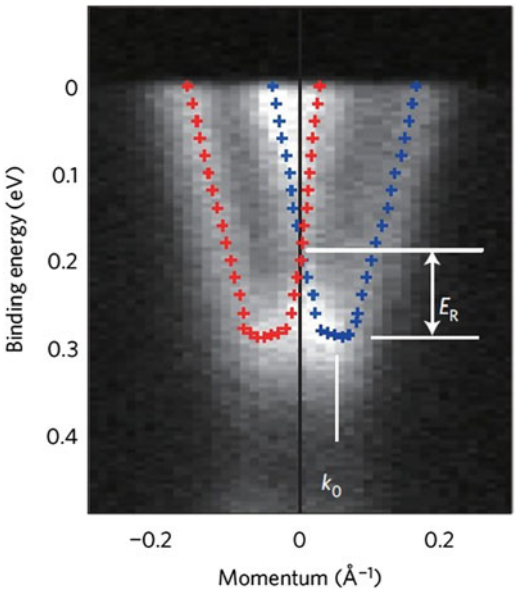

FIG. 5. Rasha splitting in BiTeI. Reproduced with permission from Ref. 12.

measurements.[111] In 2013, Eremeev et al.[112] using the density functional theory studied the bulk and surface states of BiTeBr. It was found that the ordered BiTeBr is more energetically preferable than the disordered phases according to relativistic ab initio calculations. Both Te-terminated and Br-terminated BiTeBr showed surface states with giant spin–orbit spin splitting due to potential bending within the near-surface layers. The Te-terminated surface states could be identified as Rashba-split states with a coupling parameter of 2 eV Å. These states had larger a Rashba splitting and a wider band gap than those of BiTeCl and larger splitting off from the bulk conduction band and more isotropic energy dispersion within the band gap compared with BiTeI.

Recently, it was shown that the perovskite halide may also carry Rashba splitting. In 2014, Kim et al.[113] theoretically proposed an organic–inorganic hybrid metal halide perovskite AMX_3 (A = CH_3NH_3, M = Pb and Sn, X = I and Br) as a promising ferroelectric Rashba material. It was shown that the ferroelectric switching which resulted from changing external electric fields could be used to control the helical direction of the angular momentum texture in the Rashba band. Theoretical calculations confirmed the direct coupling between $S = 1/2$ and $J = 1/2$ Rashba bands and ferroelectric polarization at valence and conduction band edges. In these hybrid halides, ferroelectric polarizations generated two distinct Rashba bands with different spin and orbital angular momentums. Meanwhile, Alessandro Stroppa et al.[9] used density function theory simulations and symmetry analysis to investigate a new low-energy structure for lead-free perovskite iodide $FASnCl_3$ with a planar formamidimium cation FA = $(NH_2CHNH_2)^+$. It was shown that this material possessed a highly tunable ferroelectricity which was of interest for multistate logic and strong spin–orbit coupling which gave rise to the coexistance of Rashba and Dresselhaus effects. At low temperatures, the ferroelectric polarization can be induced and tuned in both magnitude and direction. The coexistence of Rashba and Dresselhaus effects in $FASnI_3$ may be manipulated by an electric field that changes the ferroelectric state, giving rise to unique optical and electronic properties and new features for novel optoelectronic and spintronic devices.

J. Ferroelectricity

The existence of ferroelectricity in metal halides was initially revealed in SbSI crystals. In 1962, Fatuzzo et al.[114] studied the ferroelectric properties of SbSI crystals. In the form of an orthorhombic structure, the single crystal of this V–VI–VII compound had the shape of a thin needle with the *c*-axis being the needle axis. Dielectric constant measurements were performed to investigate the samples' ferroelectric properties. It was found that SbSI had a Curie temperature of 295 K and a high spontaneous polarization of 25 $\mu C/cm^2$ with a small coercive field strength of 100 V/cm at 273 K. The ferroelectric axis was the needle axis (*c*-axis). As the temperature increased, the polarization decreased and suddenly dropped to zero at the Curie point, indicating a first order transition.

Recently, significant interests have been emerging in the perovskite or perovskite-inspired halides.[115–126] In 2014, Pilania and Lookman[127] used first-principles based density-functional theory computations to investigate the geometry and electronic structure of $RbHgF_3$. It was shown that $RbHgF_3$ with *Pnma* space group can accommodate epitaxial compressive and tensile strains by tilting and rotation of HgF_2 octahedrals. These octahedral rotations resulted in Rb-site antipolar displacements, thus creating an A-site cation ordering in fluoroperovskite superlattices along [001] direction. The coupling between octahedral rotations and cation antipolar modes gave rise to net polarizations of 4.39 $\mu C/cm^2$ and 1.70 $\mu C/cm^2$ in $RbHgF_3/NaHgF_3$ and $RbHgF_3/KHgF_3$ superlattices, respectively. In 2015, Pilania and Uberuaga[128] studied the electronic structure, energies of cation ordering, and the biaxial strain effect on a newly designed double perovskite $CsRbCaZnCl_6$ by first-principles calculations based on density functional theory. Two ABX_3 constituents were chosen to form the double perovskite: $CsCaCl_3$, which was thermodynamically stable with a cubic perovskite structure but was not not strain sensitive and $RbZnCl_3$, which was unstable in the perovskite phase but ultra-sensitive to the epitaxial strain in this phase. When combined together, these two compounds interacted synergistically and resulted in a stable perovskite phase with a high strain response. The calculations predicted a layer-ordering for the A-site cation and a rock salt-type ordering for the B-site cation. It was shown that the electronic structure and band gap were mainly affected by the B-site instead of the A-site cation ordering. The theoretical calculations proposed a possible a phase transition from a paraelectric ground state to an antiferroelectric state that can be realized by an experimentally achievable compressive epitaxial strain of about 2.5%. Since the energy barrier of transition from the antiferroelectric state to the ferroelectric state was estimated to be only about 24 meV/f.u. for 3% compressive strain, it was possible for the material to switch to the metastable ferroelectric state.

In 2015, Liao et al.[8] investigated layered perovskite $(benzylammonium)_2PbCl_4$ and showed that it was ferroelectric with semiconducting behaviors (Fig. 6). Small crystals of the sample were obtained by mixing $PbCl_2$ and benzylammonium chloride stoichiometrically in concentrated HCl solution. Larger crystals were produced by a slowly evaporating *N*,*N*-dimethylformamide solution at 363 K. The ferroelectric property of the sample was

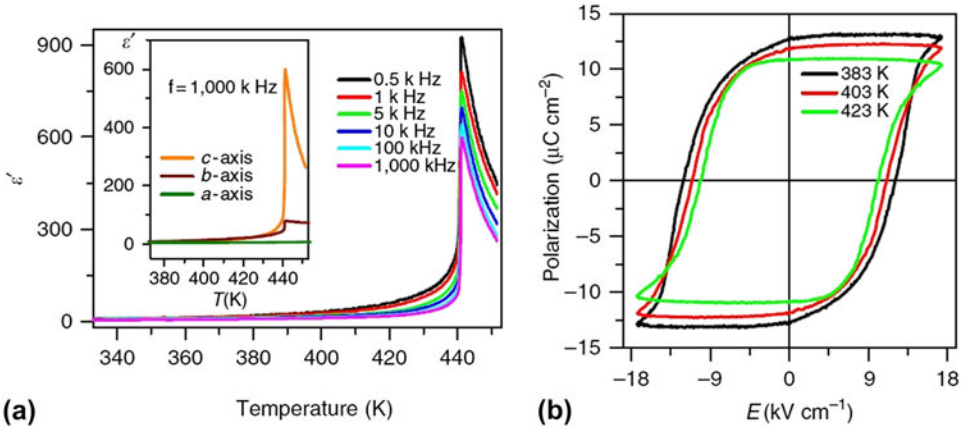

FIG. 6. Ferroelectricity in layered perovskite (benzylammonium)$_2$PbCl$_4$. Reproduced with permission from Ref. 8.

measured by the polarization electric field (P-E) hysteresis loop above 383 K. It was shown that the sample had a saturated polarization of about 13 μC/cm^2 with a relatively high coercive field, and its remnant polarization was almost equal to the saturated one. The Curie temperature was 438 K and a band gap of 3.65 eV was measured by optical ultraviolet-visible absorption spectrum. The experimental results demonstrated the material to possess high-temperature molecular ferroelectric properties and semiconducting behaviors. High-mobility ferroelectric semiconducting is always a demanded material property for developing high-performance photo-ferroelectric memory/photovoltaic devices.

III. VAPOR PHASE EPITAXY

The exploration of these interesting properties of metal halides and their applications at the device/circuit level demand high quality materials, mostly at a reduced dimension such as a nanowire, a monolayer, and a thin film. Vapor phase epitaxy, already proved in the semiconductor industry, can produce materials with the desired morphology and crystal quality. This section thus reviews the knowledge collected in the past on growing metal halides via vapor phase epitaxy, which is categorized by the crystal structures of grown materials and the types of epitaxial substrates. Table I summaries the major parameters in vapor phase epitaxy and in growth results. Among all these growth approaches, two major mechanisms have been extensively explored: chemical epitaxy and van der Waals epitaxy (Fig. 7). In chemical epitaxy, the interactions between grown materials and substrates are strong chemical bonds, while in van der Waals epitaxy, they are weaker van der Waals interactions. To realize van der Waals epitaxy, the grown materials or substrates should be 2D materials to get rid of dangling chemical bonds.[129] In the vapor phase epitaxy of metal halides, substrates have been shown crucial. In this review, the substrates are classified into three main categories: halide insulator, semiconductor, and metal. Epitaxy can be achieved with a large lattice mismatch when growing metal halides on metals or on halide insulators. However, when growing metal halides on semiconductors such as III–V compounds, the epitaxy can only be realized when the lattice mismatch is small (<1–2%). A major reason leading to such a phenomenon could be the wetting degree between the metal halide and the substrate: better wetting is always found between the metal halide and metal/halide insulators while less wetting exists between halides and III–V or II–V compounds.

A. Rock salt structure

1. Initial exploration

As early as 1950, Schulz et al.[130] used vapor phase deposition and solution deposition to grow alkali halides on mica. It was found that when the lattice constant of the film was rather small, the halides were oriented to the smaller atomic network of mica. When it became larger, a[111] fiber structure was observed. When the lattice constant was large enough, however, the halides oriented to the larger atomic network of mica. In 1956, Shigeta[131] applied PVD to grow LiF, NaF, CaF_2, MgF_2, AlF_3, and Na_3AlF_6 on PbS, NaCl, MoS_2, and ZnS. The substrate temperature was 288, 473, 573, and 673 K, respectively. The growth yielded 23 kinds of epitaxial orientations. In 1972, Prbbitt et al.[132] applied PVD to grow NaCl on Ag/mica in which the Ag (111) plane was parallel to the mica (001). When the substrate temperature was <473 K, NaCl was polycrystalline. At 473 K, NaCl has strong (001) fiber axes. At 533 K, NaCl has a triple-positioned structure, with an orientation of NaCl $[\bar{1}10]||$Ag $[1\bar{1}0]$.

2. Epitaxy on metals

In 2000s, Kiguchi et al.[133] applied MBE to synthesize alkali halide thin films on FCC structure metal substrates. They investigated the growth of LiCl on Ni (001), LiCl

TABLE I. A summary of key results on the vapor phase epitaxy of metal halides.

Deposition	Material	Substrate	Epi plane & direction	Lattice mismatch (%)	Substrate temperature	Morphology	Characterization	Reference
MBE	LiCl	Cu (001)	LiCl [100]‖Cu [110]	First-NN interatomic distance 2.9	300, 420 K	Thin film	RHEED	133
MBE	LiCl	Ni (001)	LiCl [100]‖Ni [110]	First-NN interatomic distance −11.2	300, 420 K	Thin film	RHEED	133
MBE	LiCl	Ag (001)	LiCl [100]‖Ag [100]	First-NN interatomic distance 13.2	300, 420 K	Thin film	RHEED	133
MBE	NaCl	Cu (001)	NaCl [100]‖Cu [100]	First-NN interatomic distance 10.3	300, 420 K	Thin film	RHEED	133
MBE	NaCl	Ag (001)	NaCl [100]‖Ag [100]	First-NN interatomic distance −2.4	300, 420 K	Thin film	RHEED	133
MBE	$NaCl_{0.6}Br_{0.4}$	Ag (001)	$NaCl_{0.6}Br_{0.4}$ [100]‖Ag [100]	First-NN interatomic distance 0	300, 420 K	Thin film	RHEED	133
PVD	NaCl	Cu (211)	NaCl (100)‖copper (311)	...	>300 K	Stripes	LEED STM	134
PVD	KCl	Cu (211)	KCl [010]‖Cu [01$\bar{1}$]	...	300 K	Thin film	LEED	135
PVD	RbI	Cu (211)	RbI [011]‖Cu [01$\bar{1}$]	...	310 K	Thin film	LEED	135
CVD	NaCl	Al (100)	NaCl (111)‖Al (100)	...	...	Bulk islands	STM LEED	138
CVD	NaCl	Al (111)	NaCl (111)‖Al (111)	...	...	Bulk islands	STM LEED	138
PVD	NaCl	Cu (111)	NaCl (001)‖Cu (111), NaCl [100]‖ Cu [1$\bar{1}$0]	...	355 K	Thin film	LEED	136 and 137
PVD	NaCl	Cu (311)	NaCl [110]‖Cu [01$\bar{1}$]	...	400–570 K	Thin film	LT-STM	141
PVD	LiCl	Cu (001)	LiCl [100]‖Cu [110]	...	300 K	Thin film	RHEED, AES	143
PVD	LiCl	Cu (001)	LiCl [100]‖Cu [100] and LiCl [100]‖ Cu [110]	...	>470 K	Thin film	RHEED, AES	143
MBE	NaCl	NaCl (100)	Homoepitaxy	0	−150 °C	Single crystals	RHEED X-ray Bragg scan	145 and 146
MBE	NaBr	NaBr (100)	Homoepitaxy	0	−150 °C	Single crystals	RHEED X-ray Bragg scan	145 and 146
MBE	NaI	NaI (100)	Homoepitaxy	0	−150 °C	Single crystals	RHEED X-ray Bragg scan	145 and 146
MBE	KCl	KCl (100)	Homoepitaxy	0	−150 °C	Single crystals	RHEED X-ray Bragg scan	145 and 146
MBE	KI	KI (100)	Homoepitaxy	0	−150 °C	Single crystals	RHEED X-ray Bragg scan	145 and 146
MBE	RbCl	RbCl (100)	Homoepitaxy	0	−150 °C	Single crystals	RHEED X-ray Bragg scan	145 and 146
MBE	RbI	RbI (100)	Homoepitaxy	0	−150 °C	Single crystals	RHEED X-ray Bragg scan	145 and 146
MBE	LiF	LiF (100)	Homoepitaxy	0	−150 °C	Single crystals	RHEED X-ray Bragg scan	145 and 146
MBE	KCl	RbCl (100)	RbCl (100)‖KCl (100)	4.7	200 °C	Single crystals	RHEED X-ray Bragg scan	145 and 146
MBE	NaCl	KCl (100)	KCl (100)‖NaCl (100)	10.5	200, −60 °C	Single crystals	RHEED X-ray Bragg scan	145 and 146
MBE	KBr	NaCl	KBr (100)‖NaCl (100)	14.6	0 °C	Single crystals	RHEED X-ray Bragg scan	145 and 146
MBE	RbCl	NaCl	RbCl (100)‖NaCl (100)	15.2	200 °C	Single crystals	RHEED X-ray Bragg scan	145 and 146
MBE	KF	NaCl (100)	KF (100)‖NaCl (100)	5	250 °C	Single crystals	RHEED X-ray Bragg scan	145 and 146

(continued)

TABLE I. A summary of key results on the vapor phase epitaxy of metal halides. (continued)

Deposition	Material	Substrate	Epi plane & direction	Lattice mismatch (%)	Substrate temperature	Morphology	Characterization	Reference
MBE	KF	KCl (100)	KF (100)‖KCl (100)	12	200 °C	Single crystals	RHEED X-ray Bragg scan	145 and 146
MBE	KBr	Sapphire (α-Al_2O_3) (0001)	KBr (111)‖Al_2O_3 (0001)	...	...	Single crystals	RHEED X-ray Bragg scan	145 and 146
MBE	RbF–RbI	RbCl (100)	Non-epitaxy	0	100 °C	Single crystals	RHEED X-ray Bragg scan	145 and 146
MBE	LiBr	Si (001) 2 × 1	(001)‖(001) & [100]‖[100]	1.1	...	Thin film	RHEED	149
MBE	NaCl	Si (001) 2 × 1	Non-epitaxy	(First-NN interatomic distance) 3.7	...	...	RHEED	149
MBE	LiBr	H-terminated	Epitaxy in small domian	...	...	...	RHEED	149
MBE	LiBr	Si (111) 7 × 7	(111)‖(111) & $[1\bar{1}0]$‖$[1\bar{1}0]$	...	...	Pyramidal with (001) facets	RHEED	149
MBE	NaCl	GaAs (001) 1 × 1	(001)‖(001) & [100]‖[100]	0.4	150 °C	Thin film	RHEED	149
MBE	KBr	GaAs (001) 1 × 1	Non-epitaxy	First-NN interatomic distance 16.7	...	...	RHEED	149
MBE	LiF	GaAs (001) 1 × 1	Non-epitaxy	First-NN interatomic distance 28.9	...	...	RHEED	149
MBE	NaF	GaAs (001) 1 × 1	Non-epitaxy	First-NN interatomic distance 18.3	...	...	RHEED	149
MBE	NaCl	S-terminated	Non-epitaxy	...	...	...	RHEED	149
MBE	NaCl	GaAs (111) Ga 2 × 2	(111)‖(111) & $[1\bar{1}0]$‖$[1\bar{1}0]$	...	...	Pyramidal with (001) facets	RHEED	149
MBE	NaCl	GaAs $(\bar{1}\bar{1}\bar{1})$ as 1 × 1	(111)‖$(\bar{1}\bar{1}\bar{1})$ & $[1\bar{1}0]$‖$[1\bar{1}0]$	...	...	Pyramidal with (001) facets	RHEED	149
MBE	NaCl	GaAs (100)	Non-epitaxy	First-NN interatomic distance 0.4	300 K	...	RHEED EPMA	150
MBE	NaCl	GaAs (100)	NaCl (100)‖GaAs (100)	0	420 K	Thin film	RHEED EPMA	150
MBE	$NaCl_{0.94}Br_{0.06}$	GaAs (100)	$NaCl_{0.94}Br_{0.06}$ (100)‖GaAs (100)	0	300 K	Thin film	RHEED EPMA	150
MBE	$NaCl_{0.94}Br_{0.06}$	GaAs (100)	Non-epitaxy	First-NN interatomic distance 0.4	420 K	...	RHEED EPMA	150
MBE	KCl	KBr (001)	KCl [100]‖KBr [100]	4.7	...	Thin film	EXAFS	151
Vapor phase deposition & solution deposition	KF	Mica	LiCl (111)‖mica (0001) oriented to the larger atomic network of mica	>30	...	Thin film	Electron-diffraction patterns	130
Vapor phase deposition & solution deposition	LiCl	Mica	LiCl (111)‖mica (0001)	30	...	Fiber structure	Electron-diffraction patterns	130
Vapor phase deposition & solution deposition	NaF	Mica	LiCl (111)‖mica (0001)	10–30	...	Fiber structure	Electron-diffraction patterns	130
Vapor phase deposition & solution deposition	LiF	Mica	LiCl (111)‖mica (0001) oriented to the smaller atomic network of mica	<10	...	Thin film	Electron-diffraction patterns	130
Vapor phase deposition	NaCl	Cu (211)	NaCl (001)‖Cu (311) & NaCl [110]‖Cu $[2\bar{3}\bar{3}]$	Along NaCl [110]‖Cu $[2\bar{3}\bar{3}]$ 1.7	300–600 K	Stripes	SPALEED and STM	142

(continued)

TABLE I. A summary of key results on the vapor phase epitaxy of metal halides. (continued)

Deposition	Material	Substrate	Epi plane & direction	Lattice mismatch (%)	Substrate temperature	Morphology	Characterization	Reference
PVD	LiF	GaAs (100)	Non-epitaxy	28.80	300 K	Thin film	LEED photoelectron core-level spectra	147
PVD	RbF	GaAs (100)	RbF (100)‖GaAs (100)	0.20	300 K	Thin film	LEED photoelectron core-level spectra	147
MBE	RbF/GaAs (100) (111)		Epitaxy observed	First-NN interatomic distance 0.1	300 °C, then annealed to 400 °C	Thin film	LEED, RHEED, SRPE spectrum	148
MBE	Ge/RbF		Epitaxy observed	First-NN interatomic distance 0.2	100 °C, then annealed to 400 °C	Thin film	LEED, RHEED, SRPE spectrum	148
PVD	KCl	KBr (001)	Epitaxy observed	First-NN interatomic distance −4.6	300 K	Thin film	RHEED and EEL spectrum	152
PVD	KCl	NaBr (001)	Epitaxy observed	First-NN interatomic distance 5.6	300 K	Thin film	RHEED and EEL spectrum	152
PVD	NaCl	NaBr (001)	Epitaxy observed	First-NN interatomic distance −5.6	300 K	Thin film	RHEED and EEL spectrum	152
PVD	KBr	KCl (001)	Epitaxy observed	First-NN interatomic distance 4.9	300 K	Thin film	RHEED and EEL spectrum	152
PVD	NaBr	KCl (001)	Epitaxy observed	First-NN interatomic distance −5.3	300 K	Thin film	RHEED and EEL spectrum	152
PVD	LiCl	Cu (001)	LiCl (001)‖Cu (001)	...	...	Thin film	AES, EELS and UPS	144
PVD	Ag/NaCl/Ag/mica		Ag (111)‖mica (001) NaCl is polycrystalline	...	<200 °C	Thin film	Dielectricity properties	132
PVD	Ag/NaCl/Ag/mica		Ag (111)‖mica (001)	...	200 °C	(001) fiber	Dielectricity properties	132
PVD	Ag/NaCl/Ag/mica		Ag (111)‖mica (001), NaCl $[\bar{1}10]$‖Ag $[1\bar{1}0]$	...	260 °C	Thin film	Dielectricity properties	132
PVD	NaCl	NaCl (001)	Homoepitaxy	0	−120, 25, and 120 °C	Thin film	*In situ* RHEED, SEM and AFM	153
PVD	LiF	PbS (100)	Mostly: $(100)_{film}‖(100)_{substrate}$ & $[011]_{film}‖[001]_{substrate}$ Some: $(110)_{film}‖(100)_{substrate}$ & $[001]_{film}‖[011]_{substrate}$ A few: $(100)_{film}‖(100)_{substrate}$ & $[001]_{film}‖[001]_{substrate}$	−5 −33, −5 −33	15 °C	Thin film	RHEED	131
PVD	LiF	PbS (100)	Mostly: $(100)_{film}‖(100)_{substrate}$ & $[011]_{film}‖[001]_{substrate}$ Some: $(100)_{film}‖(100)_{substrate}$ & $[001]_{film}‖[001]_{substrate}$ A few: $(110)_{film}‖(100)_{substrate}$ & $[001]_{film}‖[011]_{substrate}$	−5 −33 −33, −5	200 °C	Thin film	RHEED	131

(continued)

TABLE I. A summary of key results on the vapor phase epitaxy of metal halides. (continued)

Deposition	Material	Substrate	Epi plane & direction	Lattice mismatch (%)	Substrate temperature	Morphology	Characterization	Reference
PVD	LiF	PbS (100)	$(100)_{film}\|\|(100)_{substrate}$ & $[011]_{film}\|\|[001]_{substrate}$, or $(100)_{film}\|\|(100)_{substrate}$ & $[001]_{film}\|\|[001]_{substrate}$	−5; −33	300 °C	Thin film	RHEED	131
PVD	LiF	PbS (100)	$(100)_{film}\|\|(100)_{substrate}$ & $[001]_{film}\|\|[001]_{substrate}$	−33	400 °C	Thin film	RHEED	131
PVD	LiF	NaCl (100)	$(100)_{film}\|\|(100)_{substrate}$ & $[001]_{film}\|\|[001]_{substrate}$	−29	15–200 °C	Thin film	RHEED	131
PVD	LiF	NaCl (100)	$(100)_{film}\|\|(100)_{substrate}$ & $[001]_{film}\|\|[001]_{substrate}$, or $(110)_{film}\|\|(100)_{substrate}$ & $[001]_{film}\|\|[011]_{substrate}$	−29; −29, 1	300 °C	Thin film	RHEED	131
PVD	LiF	NaCl (100)	Mostly: $(100)_{film}\|\|(100)_{substrate}$ & $[001]_{film}\|\|[001]_{substrate}$, or $(110)_{film}\|\|(100)_{substrate}$ & $[001]_{film}\|\|[011]_{substrate}$	−29; −29, 1	400 °C	Thin film	RHEED	131
PVD	LiF	NaCl (100)	A few: $(100)_{film}\|\|(100)_{substrate}$ & $[011]_{film}\|\|[001]_{substrate}$	1				
PVD	LiF	MoS_2 (0001)	$(100)_{film}\|\|(0001)_{substrate}$	...	15 °C	Thin film	RHEED	131
PVD	LiF	MoS_2 (0001)	$(100)_{film}\|\|(0001)_{substrate}$ & $[011]_{film}\|\|[2\bar{1}\bar{1}0]_{substrate}$, or $(100)_{film}\|\|(0001)_{substrate}$	−9, 4	200–400 °C	Thin film	RHEED	131
PVD	LiF	ZnS (110)	$(100)_{film}\|\|(110)_{substrate}$ & $[001]_{film}\|\|[001]_{substrate}$	4, −26	15 °C	Thin film	RHEED	131
PVD	LiF	ZnS (110)	$(113)_{film}\|\|(110)_{substrate}$ & $[1\bar{1}0]_{film}\|\|[001]_{substrate}$	11, −13	200–300 °C	Thin film	RHEED	131
PVD	LiF	ZnS (110)	$(100)_{film}\|\|(110)_{substrate}$ & $[011]_{film}\|\|[001]_{substrate}$	−27, 4	400 °C	Thin film	RHEED	131
PVD	LiF	ZnS (110)	Complicated	...	450 °C	Thin film	RHEED	131
PVD	NaF	PbS (100)	$(100)_{film}\|\|(100)_{substrate}$ & $[001]_{film}\|\|[001]_{substrate}$	−23	27 °C	Thin film	RHEED	131
PVD	NaF	PbS (100)	$(100)_{film}\|\|(100)_{substrate}$ & $[001]_{film}\|\|[001]_{substrate}$, or $(100)_{film}\|\|(100)_{substrate}$ & $[011]_{film}\|\|[001]_{substrate}$	−23; 9	100 °C	Thin film	RHEED	131
PVD	NaF	PbS (100)	$(100)_{film}\|\|(100)_{substrate}$ & $[001]_{film}\|\|[001]_{substrate}$, or $(100)_{film}\|\|(100)_{substrate}$	−23	200 °C	Thin film	RHEED	131
PVD	NaF	PbS (100)	$(100)_{film}\|\|(100)_{substrate}$ & $[001]_{film}\|\|[001]_{substrate}$	−23	300 °C	Thin film	RHEED	131
PVD	NaF	NaCl (100)	$(100)_{film}\|\|(100)_{substrate}$ & $[001]_{film}\|\|[001]_{substrate}$	−19	27–300 °C	Thin film	RHEED	131
PVD	NaF	NaCl (100)	Trace	...	400 °C	Thin film	RHEED	131
PVD	NaF	MoS_2 (0001)	$(100)_{film}\|\|(0001)_{substrate}$	...	27–300 °C	Thin film	RHEED	131
PVD	NaF	ZnS (110)	$(111)_{film}\|\|(110)_{substrate}$ & $[1\bar{1}0]_{film}\|\|[001]_{substrate}$, or $(311)_{film}\|\|(100)_{substrate}$	−15, 4; −15, −1	27 °C	Thin film	RHEED	131

(continued)

TABLE I. A summary of key results on the vapor phase epitaxy of metal halides. (continued)

Deposition	Material	Substrate	Epi plane & direction	Lattice mismatch (%)	Substrate temperature	Morphology	Characterization	Reference
PVD	NaF	ZnS (110)	$(111)_{film}\|\|(110)_{substrate}$ & $[1\bar{1}0]_{film}\|\|[001]_{substrate}$	−15, 4	100–300 °C	Thin film	RHEED	131
PVD	Na_3AlF_6	PbS (100)	$(110)_{film}\|\|(100)_{substrate}$ & $[001]_{film}\|\|[011]_{substrate}$	−8	270 °C	Thin film	RHEED	131
PVD	Na_3AlF_6	NaCl (100)	$(110)_{film}\|\|(100)_{substrate}$ & $[001]_{film}\|\|[011]_{substrate}$	−3	300 °C	Thin film	RHEED	131
PVD	Na_3AlF_6	MoS_2 (0001)	$(011)_{film}\|\|(0001)_{substrate}$ & $[100]_{film}\|\|[10\bar{1}0]_{substrate}$	−1, 1	200–400 °C	Thin film	RHEED	131
PVD	Na_3AlF_6	ZnS (110)	$(110)_{film}\|\|(110)_{substrate}$ & $[001]_{film}\|\|[001]_{substrate}$, or $(110)_{film}\|\|(110)_{substrate}$ & $[1\bar{1}0]_{film}\|\|[001]_{substrate}$, or $(\bar{3}12)_{film}\|\|(110)_{substrate}$ & $[111]_{film}\|\|[001]_{substrate}$, or $(100)_{film}\|\|(110)_{substrate}$ & $[010]_{film}\|\|[001]_{substrate}$, or $(221)_{film}\|\|(110)_{substrate}$, or $(0\bar{1}1)_{film}\|\|(110)_{substrate}$ & $[100]_{film}\|\|[1\bar{1}0]_{substrate}$, or $(112)_{film}\|\|(110)_{substrate}$ & $[1\bar{1}0]_{film}\|\|[1\bar{1}0]_{substrate}$	1, 43; 1, 43; −12, 1; 8, −1; 1; −7, −14; 1, 1	300–450 °C	Thin film	RHEED	131
PVD	CaF_2	PbS (100)	Non-epitaxy	...	300–400 °C	Thin film	RHEED	131
PVD	CaF_2	NaCl (100)	Non-epitaxy	...	400 °C	Thin film	RHEED	131
PVD	CaF_2	MoS_2 (0001)	$(111)_{film}\|\|(0001)_{substrate}$ & $[1\bar{1}0]_{film}\|\|[2\bar{1}\bar{1}0]_{substrate}$	23	300–400 °C	Thin film	RHEED	131
PVD	CaF_2	ZnS (110)	$(110)_{film}\|\|(110)_{substrate}$ & $[1\bar{1}0]_{film}\|\|[001]_{substrate}$	0	400 °C	Thin film	RHEED	131
PVD	MgF_2	PbS (100)	Non-epitaxy	...	300–400 °C	Thin film	RHEED	131
PVD	MgF_2	NaCl (100)	Non-epitaxy	...	400 °C	Thin film	RHEED	131
PVD	MgF_2	MoS_2 (0001)	Non-epitaxy	...	400 °C	Thin film	RHEED	131
PVD	MgF_2	ZnS (110)	Non-epitaxy	...	400 °C	Thin film	RHEED	131
PVD	AlF_3	PbS (100)	Non-epitaxy	...	270 °C	Thin film	RHEED	131
PVD	AlF_3	NaCl (100)	Non-epitaxy	...	270–400 °C	Thin film	RHEED	131
PVD	AlF_3	MoS_2 (0001)	Non-epitaxy	...	400 °C	Thin film	RHEED	131
PVD	AlF_3	ZnS (110)	Non-epitaxy	...	400 °C	Thin film	RHEED	131
CVD	β-AgI	Mica	Epitaxy observed	...	40 °C	Layer	Electron micrograph and diffraction pattern	155
CVD	β-AgI	Glass	Non-epitaxy	...	40 °C	...	Electron micrograph and diffraction pattern	155
CVD	β-AgI	Ag (001)	AgI (0001)||Ag (001) & AgI $[11\bar{2}0]$||Ag [100]	Along AgI $[11\bar{2}0]$||Ag [100] 2.8	80 °C	Thin irregular AgI crystals	TEM, SAED	154

(continued)

TABLE I. A summary of key results on the vapor phase epitaxy of metal halides. (continued)

Deposition	Material	Substrate	Epi plane & direction	Lattice mismatch (%)	Substrate temperature	Morphology	Characterization	Reference
CVD	β-AgI	Ag (001)	AgI (0001)‖Ag (001) & AgI [11$\bar{2}$0]‖Ag [100]	Along AgI [11$\bar{2}$0]‖Ag [100] 2.8	200 °C	Parallelograms and several extremely long needle-like shape	TEM, SAED	154
CVD	β-AgI	Ag (011)	AgI (0001)‖Ag (001) & AgI [10$\bar{1}$0]‖Ag [100]	Along AgI [10$\bar{1}$0]‖Ag [100] 2.8	80 °C	Thin irregular AgI crystals	TEM, SAED	154
CVD	β-AgI	Ag (011)	AgI (0001)‖Ag (001) & AgI [10$\bar{1}$0]‖Ag [100]	Along AgI [10$\bar{1}$0]‖Ag [100] 2.8	200 °C	Parallelogram-shaped and needle-like shape	TEM, SAED	154
CVD	β-AgI	Ag (111)	AgI (0001)‖Ag (001) & AgI [10$\bar{1}$0]‖Ag [110]	Along AgI [10$\bar{1}$0]‖Ag [110] 3.2	80 °C	Thin irregular AgI crystals	TEM, SAED	154
CVD	β-AgI	Ag (111)	AgI (0001)‖Ag (001) & AgI [10$\bar{1}$0]‖Ag [110]	Along AgI [10$\bar{1}$0]‖Ag [110] 3.2	200 °C	Well-shaped hexagonal at 200 C	TEM, SAED	154
PVD	AgCl	Mica	AgCl (111)‖mica (0001)	...	Can be achieved in a wide range	Thin film	TEM	156
PVD	AgCl	NaCl	AgCl (200)‖NaCl (001)	...	Can be achieved in a wide range	Thin film	TEM	156
PVD	AgBr	Mica	AgBr (111)‖mica (0001)	...	Can be achieved in a wide range	Thin film	TEM	156
PVD	AgBr	NaCl	AgBr (200)‖NaCl (001)	...	Can be achieved in a wide range	Thin film	TEM	156
PVD	AgI	Mica	β-AgI (0001)‖mica (0001) α/γ-AgI (111)‖mica (0001)	...	100–150 °C	Thin film	TEM	156
PVD	AgI	NaCl	β-AgI (0001)‖NaCl (200) α/γ-AgI (111)‖NaCl (200)	...	100–150 °C	Thin film	TEM	156
MBE	CaF_2	GaAs (001)	Epitaxy observed	...	420 °C	Thin film	RHEED	158
MBE	CaF_2	GaAs (001)	Non-epitaxy	...	580 °C	...	RHEED	158
MBE	CaF_2	Si (111)	CaF_2 (111)‖Si (111) CaF_2 [1$\bar{1}$0]‖Si [1$\bar{1}$0]	...	<600 °C	Pyramids	RHEED	165
MBE	CaF_2	Si (111)	CaF_2 (001)‖Si (111)	...	>600 °C	Thin film	RHEED	165
MBE	CaF_2	Si (001)	Epitaxy observed	...	<550 °C	Dot	RHEED	165
MBE	CaF_2	Si (001)	CaF_2 (110)‖Si (001) CaF_2 [1$\bar{1}$0]‖Si [1$\bar{1}$0]	45% across the wire	>700 °C	Wire/wetting layer epitaxial formation	RHEED	165
MBE	CdF_2	Si (111)	CdF_2 (111)‖Si (111) CdF_2 [1$\bar{1}$0]‖Si [1$\bar{1}$0]	...	<350 °C	Pyramids	RHEED	165
MBE	CdF_2	Si (111)	CdF_2 (001)‖Si (111)	...	>350 °C	Thin film	RHEED	165

(continued)

TABLE I. A summary of key results on the vapor phase epitaxy of metal halides. (continued)

Deposition	Material	Substrate	Epi plane & direction	Lattice mismatch (%)	Substrate temperature	Morphology	Characterization	Reference
PVD	CaF_2	GaAs (100)	Epitaxy observed	...	460–590 °C	Mono epitaxial layer	Photoemission spectra	160
MBE	(CaSr) F_2 (actually $Ca_{0.55}Sr_{0.45}F_2$)	GaAs (111)	Epitaxy observed	0	Reduced from 700 to 450 °C	Thin film	C–V curve, ICTS	161
MBE	$Ca_{0.43}Sr_{0.57}F_2$	GaAs (100)	Epitaxy observed	...	325 °C	Island	Synchrotron radiation photoemission and RHEED	162
PVD	Ge (001)/CaF_2/Ni (001)		CaF_2 [110]‖Ni [100] & CaF_2 [$\bar{1}$10]‖Ni [010]	3.2 between Ge and CaF_2	350 °C, 400 °C, respectively	Layer	...	157
PVD	BaF_2	GaAs (100), (111) and (011)	Epitaxy observed	...	500–700 °C	Layer	XPS and RHEED	163
MBE	CaF_2 (100)/Si (100) In the growth of: CdTe (100)/BaF_2 (100)/CaF_2 (100)/Si (100)		CaF_2 (100)‖Si (100)	CaF_2 (100) and Si (100) have a lattice mismatch of 0.6	550 °C	Thin film	RHEED	166
MBE	BaF_2 (100)/CaF_2 (100) In the growth of: CdTe (100)/BaF_2 (100)/CaF_2 (100)/Si (100)		BaF_2 (100)‖CaF_2 (100)	BaF_2 (100) and CaF_2 (100) have a lattice mismatch of 14	First 550 °C, and then annealed to 700 °C	Thin film	RHEED	166
MBE	CdTe (100)/BaF_2 (100) In the growth of: CdTe (100)/BaF_2 (100)/CaF_2 (100)/Si (100)		CdTe (100)‖BaF_2 (100)	CdTe (100)/and BaF_2 (100) have a lattice mismatch of 4.5	200–350 °C	Thin film	RHEED	166
PVD	CaF_2	On NaCl (100)	Non-epitaxy	...	Room temperature	...	Micrographs and diffraction patterns	167
PVD	CaF_2	On NaCl (100)	CaF_2 (110)‖NaCl (100), and CaF_2 ⟨111⟩‖NaCl ⟨100⟩	...	150 °C	Thin film	Micrographs and diffraction patterns	167
PVD	CaF_2	On NaCl (100)	CaF_2 (110)‖NaCl (100), and CaF_2 ⟨111⟩‖NaCl ⟨100⟩	...	250 °C	Thin film	Micrographs and diffraction patterns	167
PVD	CaF_2	On NaCl (100)	CaF_2 (100)‖NaCl (100), and CaF_2 ⟨110⟩‖NaCl ⟨100⟩	...	350 °C	Thin film	Micrographs and diffraction patterns	167
PVD	CaF_2	On NaCl (100)	Epitaxy observed	...	500 °C	Thin film	Micrographs and diffraction patterns	167
MBE	CaF_2	InP (001)	CaF_2 (001)‖InP (001)	−6.5	650 K	Thin film	LEED and AFM	164
MBE	SrF_2	InP (001)	...	−1.2	650 K	Thin film	LEED and AFM	164
PVD	CuCl	GaAs	Epitaxy observed	−4	...	Thin film	RHEED, AES, EELS	170
PVD	CuBr	GaAs	Epitaxy observed	0.4	...	Thin film	RHEED, AES, EELS	170

(continued)

TABLE I. A summary of key results on the vapor phase epitaxy of metal halides. (continued)

Deposition	Material	Substrate	Epi plane & direction	Lattice mismatch (%)	Substrate temperature	Morphology	Characterization	Reference
PVD	CuI	GaAs	Epitaxy observed	6.9	...	Thin film	RHEED, AES, EELS	170
MBE	CuCl	MgO (001)	CuCl (111)‖MgO (001) & CuCl $[\bar{1}10]$‖MgO [110]	...	333 K	First triangular islands, then become layer	RHEED and AFM	171
MBE	CuCl	CaF_2 (111)	CuCl (111)‖CaF_2 (111)	...	333 K	First triangular islands, then become hexagonal-shaped islands	RHEED and AFM	171
MBE	CuCl	MgO (001)	CuCl (111)‖MgO (001) & CuCl $[1\bar{1}0]$‖MgO [110]	...	333 K	Thin film	RHEED, AFM and XRD	172
MBE	CuBr	MgO (001)	CuBr (111)‖MgO (001) & CuBr $[1\bar{1}0]$‖MgO [l00]	...	333 K	Thin film	RHEED, AFM and XRD	172
PVD	CuCl (110)	GaP (110)	CuCl (110)‖GaP (110)	First-NN interatomic distance 0.8	100 °C	Layer	LEED	169
PVD	CuCl	TiO_2 (110)	...	...	Room temperature	Thin film	UPS, EELS and AES	175
MBE	CuCl	MgO (001)	CuCl (111)‖MgO (001), & CuCl $[1\bar{1}0]$‖MgO [110], $[\bar{1}1\bar{0}]$, $[\bar{1}10]$ and $[1\bar{1}0]$ in different domain	...	333 K	Thin film	RHEED and AFM	174
MBE	CuCl	CaF_2 (111)	...	...	110 and 89 °C	Thin film	AFM and RHEED	168
MBE-VDWE	PbI_2	Mica (001)	PbI_2 [0001]‖mica [001] with an offset angle = 5, PbI_2 $[10\bar{1}0]$‖mica [310]	...	250–300 °C	Thin film	TEM, AFM, PL spectra, bending test and raman characterization	182
MBE-VDWE	PbI_2	MoS_2 (0001)	PbI_2 (0001)‖MoS_2 (0001) & PbI_2 $[10\bar{1}0]$‖MoS_2 $[2\bar{1}\bar{1}0]$	First-NN interatomic distance 44	150 °C	Thin film	RHEED	180
MBE-VDWE	PbI_2	$MoSe_2$ (0001)	PbI_2 (0001)‖$MoSe_2$ (0001) & PbI_2 $[10\bar{1}0]$‖$MoSe_2$ $[2\bar{1}\bar{1}0]$ or PbI_2 (0001)‖$MoSe_2$ (0001) & PbI_2 $[10\bar{1}0]$‖$MoSe_2$ $[10\bar{1}0]$	First-NN interatomic distance 38	150 °C	Thin film	RHEED	180
MBE-VDWE	PbI_2	$NbSe_2$ (0001)	PbI_2 (0001)‖$NbSe_2$ (0001) & PbI_2 $[2\bar{1}\bar{1}0]$ has 19° offset angle with $NbSe_2$ $[2\bar{1}\bar{1}0]$	First-NN interatomic distance 32	150 °C	Thin film	RHEED	180
MBE-VDWE	PbI_2	$TaSe_2$ (0001)	PbI_2 (0001)‖$TaSe_2$ (0001) & PbI_2 $[2\bar{1}\bar{1}0]$ has a 19° offset angle with $TaSe_2$ $[2\bar{1}\bar{1}0]$	First-NN interatomic distance 31	150 °C	Thin film	RHEED	180
MBE-VDWE	PbI_2	GaSe (0001)	PbI_2 (0001)‖GaSe (0001) & PbI_2 $[2\bar{1}\bar{1}0]$‖GaSe $[2\bar{1}\bar{1}0]$	First-NN interatomic distance 21	150 °C	Thin film	RHEED	180
CVD-VDWE	PbI_2	Se–GaAs $(\bar{1}\bar{1}\bar{1})$	PbI_2 (0001)‖GaSe (0001) & PbI_2 $[2\bar{1}\bar{1}0]$‖GaSe $[2\bar{1}\bar{1}0]$	First-NN interatomic distance 14	150 °C	Thin film	RHEED	180
Hot wall epitaxy (van der Waals)	PbI_2	CdI_2 (001)	...	First-NN interatomic distance 7.8	75–120 °C	Thin film	Absorption spectra of PbI_2	179

(continued)

TABLE I. A summary of key results on the vapor phase epitaxy of metal halides. (continued)

Deposition	Material	Substrate	Epi plane & direction	Lattice mismatch (%)	Substrate temperature	Morphology	Characterization	Reference
Hot wall epitaxy (van der Waals)	PbI_2|CdI_2 superlattices	A mica or a sapphire	...	...	358 K	Thin film	XRD	181
PVD	CdI_2	SiO_2/Si	CdI_2 (001)‖substrate (001)	...	320 °C	Nanoplates	OM, SEM, AFM, XRD, HRTEM, and SAED	176
PVD	CdI_2	WS_2	CdI_2 (001)‖substrate (001), a few CdI_2 nanoplates have an edge parallel to bottom edge of WS_2, while rest of them all have 30° offangle	...	320 °C	Nanoplates	OM, SEM, AFM, XRD, HRTEM, and SAED	176
PVD	CdI_2	WSe_2	CdI_2 (001)‖substrate (001)	...	320 °C	Nanoplates	OM, SEM, AFM, XRD, HRTEM, and SAED	176
PVD	CdI_2	MoS_2	CdI_2 (001)‖substrate (001)	...	320 °C	Nanoplates	OM, SEM, AFM, XRD, HRTEM, and SAED	176
PVD	CdI_2	InSb (001)	CdI_2 (0001)‖InSb (001), and InSb $[1\bar{1}0]$ has 7° offangle with the two domain orientations of CdI_2	...	310 K	Thin film	UPS and LEED	184
Hot wall method (van der Waals epitaxy)	BiI_3	PbI_2 (001)	...	BiI_3 on PbI_2 (001): 39	20 to 90 °C	Thin film	Exciton absorption spectra	183
Hot wall method (van der Waals epitaxy)	BiI_3	CdI_2 (001)	...	BiI_3 on CdI_2 (001): 43	20–90 °C	Thin film	Exciton absorption spectra	183
PVD	α-CsCl	MgO (001)	(001) α-CsCl‖(001) MgO & [100] α-CsCl‖[100] MgO	Between (001) α-CsCl & (001) MgO 2.1	293–673 K	Thin film	CAICASS RHEED AFM	185
PVD	β-CsCl	MgO (001)	(001) β-CsCl‖(001) MgO & [110] β-CsCl‖[100] MgO	...	293–673 K	Thin film	CAICASS RHEED AFM	185
MBE	CsCl	NaCl/GaAs (001)	CsCl (001)‖NaCl/GaAs (001), [100] CsCl‖[100] GaAs	...	470 K	Thin film	EELS RHEED AES UPS	186
MBE	CsBr	LiF (001)	Only α-CsCl was grown, (110) α-CsBr‖(001) LiF & [001] α-CsBr‖[001] LiF	4.90	300 K	Thin film	RHEED AES EELS UPS	187
MBE	CsBr	LiF (001)	Only β-CsCl was grown, (001) β-CsBr‖(001) LiF & [100] β-CsBr‖[100] LiF	77	420 K	Thin film	RHEED AES EELS UPS	187
MBE	CsBr	KBr (001)	(001) β-CsBr‖(001) KBr and [100] β-CsBr‖[100] KBr	9.50	300–500 K	Thin film	RHEED AES EELS UPS	187

(continued)

TABLE I. A summary of key results on the vapor phase epitaxy of metal halides. (continued)

Deposition	Material	Substrate	Epi plane & direction	Lattice mismatch (%)	Substrate temperature	Morphology	Characterization	Reference
CVD-VDWE	$CsPbX_3$ (X = Cl, Br, I)	Mica	PVK (011)‖mica (001), and PVK (100) has 30° off angle compared with mica (020)	...	400 °C	Sheets and rods	XRD TEM PL spectra	190
CVD-VDWE	$CsPbCl_3$	Mica	...	...	625 °C	Nanoplatelets	XRD, AFM	189
CVD-VDWE	$CsPbBr_3$	Mica	...	...	575 °C	Nanoplatelets	XRD, AFM	189
CVD-VDWE	$CsPbI_3$	Mica	...	...	550 °C	Nanoplatelets	XRD, AFM	189
CVD-VDWE	$CsPbX_3$ (X = Cl, Br, I)	Mica	$CsPbBr_3$ [001]‖mica [010] & $CsPbBr_3$ [110]‖mica [100]	Mismatch of $CsPbBr_3$ [001]‖mica [010] was 0.04, and the mismatch of $CsPbBr_3$ [110]‖mica [100] was −2.0	300–350 °C	Nanowire network	AFM, XRD and SEM	191
CVD-VDWE	$MAPbI_3$/$MAPbBr_3$ double heterojunction	Mica	$MAPbI_3$/$MAPbBr_3$ (001)‖mica (0001)	...	Around 300 °C	Films and rods	SAED, EDX and PL spectra	192
CVD-VDWE	$MAPbCl_3$	Mica	Mica (001)‖$MAPbCl_3$ (001), mica (200)‖$MAPbCl_3$ (200) (with 5° offset), and mica (020)‖perovskite (010) (with 5° offset)	...	220 °C	Thin films	TEM, SAED and AFM	188
Three-steps method	$MAPbI_3$	Graphene, MoS_2, and h-BN	...	...	120 °C	Nanoplatelets	XRD, TEM, AFM, and XRTEM	193
CVD-VDWE	$MAPbI_3$	Mica	...	...	380 °C	Platelets	XRD and PL spectra	194
Two-steps method	$MAPbX_3$ (X = Cl, Br, I)	Mica	...	...	First step: 380 °C for PbI_2, 350 °C for $PbBr_2$, and 510 °C for $PbCl_2$ Second step: the conversion temperature was 120 °C	Platelet	SEM, AFM, XRD, PL spectra	178
Two-steps method	$CH_3NH_3PbX_3$ (X = Cl, Br, or I)	SiO_2/Si	...	...	First step: for PbI2 was 30–180 °C Second step: for vapor–solid reaction was 120 °C	Nanosheet	TEM, AFM, and PL spectra	195
MBE	LaF_3 (0001)/NdF_3 (0001)/GaAs $(\bar{1}\bar{1}\bar{1})$ In the growth of: LaF_3 (0001)/Dy (001)/LaF_3 (0001)/NdF_3 (0001)/GaAs $(\bar{1}\bar{1}\bar{1})$		LaF_3 (0001)‖NdF_3 (0001)‖GaAs $(\bar{1}\bar{1}\bar{1})$	2.1 for LaF_3 on NdF_3	500 °C	Thin films	LEED	196

(continued)

TABLE I. A summary of key results on the vapor phase epitaxy of metal halides. (continued)

Deposition	Material	Substrate	Epi plane & direction	Lattice mismatch (%)	Substrate temperature	Morphology	Characterization	Reference
		LaF_3 (0001)/Dy (001)/LaF_3 (0001)						
MBE	In the growth of: LaF_3 (0001)/Dy (001)/LaF_3 (0001)/NdF_3 (0001)/GaAs ($\bar{1}\bar{1}\bar{1}$)	LaF_3 (0001)/Dy (001)/LaF_3 (0001)	LaF_3 (0001)‖Dy (001)‖LaF_3 (0001)	−0.07 for Dy on LaF_3,	300 °C	Thin films	LEED	196
	LaF_3 (0001)/GaAs ($\bar{1}\bar{1}\bar{1}$)							
	In the growth of:						GID, XPS and	197 and
MBE	LaF_3 (0001)/Rare earth metal (Dy, Er, ho) (001)/LaF_3 (0001)/GaAs ($\bar{1}\bar{1}\bar{1}$)	LaF_3 (0001)/GaAs ($\bar{1}\bar{1}\bar{1}$)	LaF_3 (0001)‖GaAs ($\bar{1}\bar{1}\bar{1}$)	…	500 °C	Thin films	SQUID	198
	LaF_3 (0001)/Rare earth metal (Dy, Er, ho) (001)/LaF_3 (0001)		LaF_3 (0001)‖rare earth metal (Dy, Er, ho) (001)‖LaF_3 (0001), and rare earth metal [100]‖LaF_3 [110]	0.03 for rare earth metal [100]‖LaF_3 [110]				
MBE	In the growth of: LaF_3 (0001)/Rare earth metal (Dy, Er, ho) (001)/LaF_3 (0001)/GaAs ($\bar{1}\bar{1}\bar{1}$)				300 °C	Thin films	GID, XPS and SQUID	197 and 198
MBE	LaF_3/Er/Dy/Er/LaF_3	LaF_3 (0001)‖Er (001)‖Dy (001)‖Er (001)‖LaF_3 (0001) and rare earth metal [100]‖LaF_3 [110]		0.03 for rare earth metal [100]‖LaF_3 [110]	300 °C	Thin films	GID, XPS and SQUID	197 and 198

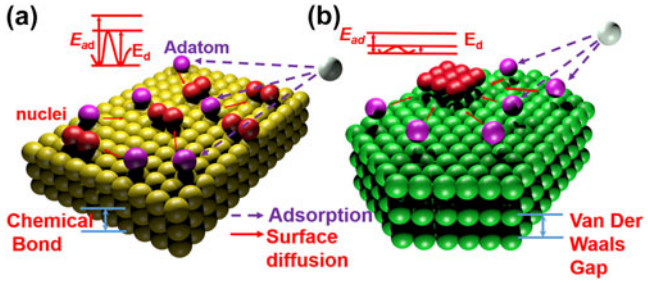

FIG. 7. (a) Chemical epitaxy. (b) van der Waals epitaxy. Reproduced with permission from Ref. 188.

on Ag (001), NaCl on Ni (001), NaCl on Cu (001), NaCl on Ag (001), and $NaCl_{0.6}Br_{0.4}$ on Ag (001). The first nearest neighbor (first-NN) interatomic distances of these five combinations differ by 2.9%, −11.2%, 13.2%, 10.3%, −2.4%, and 0.0%, respectively. Substrate temperature was at 300 and 420 K. They found that the [100] film is parallel to the [110] substrate for LiCl on Cu (001) and LiCl on Ni (001), which was called the 45° growth because of the 45° angle between the [100] film and [100] substrate, while for LiCl on Ag (001), NaCl on Cu (001), NaCl on Ag (001), and $NaCl_{0.6}Br_{0.4}$ on Ag (001), $[100]_{film}$ is parallel to $[100]_{substrate}$ (which was called 0° growth). Compared with the first-NN interatomic distances, they found that 45° growth occurred only when the distance is small, while 0° growth can happen even when the distance is very large. They believed that this can be partially explained by the weak interaction between alkali halide and the metal.

In 2000, Fölsch et al.[134] used PVD to grow NaCl on the Cu (211) substrate. The substrate temperature was at 300 K. With high-resolution low energy electron diffraction (LEED) and scanning tunneling microscope (STM), they found that, however, NaCl only grew on the (311) facets. They believed that this was due to the self-diffusion of copper to form (100)-terminated layers, as well as the optimum match of lattices between copper and sodium chloride. Meanwhile, they[135] used PVD to grow KCl (100) and RbI (100) on the Cu (211) substrate. LEED was introduced to analyze the structure of thin films. They successfully synthesized epitaxial thin films, with KCl [010]‖Cu [01$\bar{1}$] and RbI [011]‖Cu [01$\bar{1}$]. They believed that this kind of epitaxy can be attributed to the row matching between the intrinsic steps of the substrate and the lattices along the low-indexed azimuthal directions in the thin film, which is caused by the restriction of uniaxial substrate corrugation. In addition, Bennewitz et al.[136] used PVD to grow NaCl ultra-thin films on Cu (111). With LEED, they found that at 335 K, NaCl was well oriented with NaCl (001) parallel to Cu (111) and NaCl [100] parallel to Cu [1$\bar{1}$0]. They believed that the NaCl lattice was contracted by 2.1% to match four NaCl rows with five Cu rows, which was supported by the LEED result. In 2000, Bennewitz et al.[137] introduced

a more detailed and theoretical analysis on their NaCl ultra-thin film on Cu (111). Dynamic force microscopy (DFM) was used in their study. They demonstrated that NaCl contains no more than 2 layers and that the contrast in DFM images was determined by the chemical interaction, which indicated a displacement of ions on surface.

At the same time, Hebenstreit et al.[138,139] used both PVD and CVD to grow NaCl (111) on aluminum (100) and (111) substrates. Because NaCl (111) is polar, this surface was expected to be reconstructed to form a neutral and stable structure.[140] However, in this work they successfully produced unreconstructed NaCl (111) thin films by adsorption of Cl and Na on aluminum (100) and (111) with excess Na. STM and LEED were used to monitor and quantify the deposition process, as well as to reveal the ultimate (111) surface of NaCl. By ab initio calculations, they believed that Na was +1/2 charged and thin films were neutral. In 2001, Repp et al.[141] used the PVD deposition method to grow sodium chloride on Cu (311). Substrate temperature was at 400–570 K. The STM images showed that NaCl [110] is parallel to the intrinsic steps of the Cu substrate. In this case, a strong interaction between the NaCl and Cu substrate is found, while in former research, it had been shown that the interaction between NaCl and the Al substrate was weak.[139] They believed that on Cu (311), Na^+ will stay along the steps, while Cl-will stay between the steps, which corresponds to the alternant positive and negative charges on the copper substrate. This consistent stripe of opposite charges results in a strong enough electrostatic interaction, which accounts for the strong bonding between NaCl and Cu.

By following their previous attempts, in 2002, Folsch et al.[142] used PVD to grow NaCl on Cu (211) at different growth conditions. An epitaxial orientation of NaCl [110]||Cu $[2\bar{3}\bar{3}]$ was achieved. They found that NaCl and copper formed a quasi-periodic stripe structure. They believed that the formation of NaCl stripes has two requirements. First, the substrate's original orientation must have a close facet orientation that can match the film well. What's more, the mobility of the substrate surface atoms must be large enough to achieve significant mass transport to form the facet.

In 2001, Kiguchi et al.[143] used PVD method to grow LiCl on Cu (001) substrate. With reflection high energy electron diffraction (RHEED), they found that at 300 K, LiCl [100] was grown parallel to Cu [110], while two domains of LiCl films (LiCl [100]||Cu [100] and LiCl [100]||Cu [110]) were grown at temperatures higher than 470 K. They found that the growth mode was layer-by-layer, and the film thickness was five molecular layers. In 2003, Kiguchi et al.[144] applied PVD to grow LiCl (001) on Cu (001).

3. Epitaxy on semiconductors/insulators

In the 1990s, Yang et al.[145,146] applied MBE to grow several rock salt halides on different insulators. Specifically, they grew NaCl, NaBr, NaI, KCl, KI, RbCl, RbI, and LiF homoepitaxially at −150 °C and KCl, NaCl, KBr, RbCl, KF, and KF on RbCl (100), KCl (100), NaCl, NaCl, NaCl (100), KCl (100), with lattice mismatch of 4.7%, 10.5%, 14.6%, 15.2%, 5.0%, 12.0%, respectively. They found that the epitaxial growth rate of alkali halides can be tens of monolayers/second at ~100 K.

At the same time, Klauser et al.[147,148] used PVD to grow RbF and LiF on GaAs (100). The substrate was at room temperature. The lattice mismatches are 0.2% and 28.8%, respectively. LEED and photoelectron core-level spectra were used to analyze the result. They found that RbF showed an epitaxial growth of RbF (100) on GaAs (100). They believed that Ga–F bonds were formed at first, in which one F had two bonds with two Ga to form a first layer in the NaCl-type structure. In 1991, Klauser et al. also applied MBE to grow RbF as an interlayer between Ge (100) and GaAs (111). The substrate temperature was 573 K. The lattice mismatches between RbF and GaAs and RbF and Ge lattices were 0.1 and 0.2%, respectively. They found that on the interface, there were no Ga but some As, which was totally different from that of Ge/GaAs. They attributed this to the etching of F on Ga the outer layer.

In 1997, Saiki[149] used MBE to grow alkali halides on alkali halides and semiconductors. In the growth of alkali halides on alkali halides, they found that along with the change of mismatches, the RHEED images changed and can be divided into three categories, indicating different modes of growth. When the lattice mismatch was small, they saw a streak pattern with its interval changing continuously. This indicated a layer by layer growth. When the lattice mismatch was larger, a double-line streak pattern was observed at first and then the streak coming from the substrate was replaced by the streak from the overgrown materials gradually. Because double-line can be seen initially, the interactions between alkali halides were small. When the lattice mismatch was large enough, spots appeared on the substrate streak when growth started and then the weak streak connected the spots and the substrate streak faded out with the growth proceeding. Those dots indicated the island growth. They found, however, that the growth of alkali halides on the semiconductor was different from that on the metal: because of the stronger interaction between alkali halides and semiconductors, the epitaxial growth on semiconductors required a strict lattice registration. In 2002, Kiguchi et al.[150] used MBE to grow alkali halides on GaAs (100). They grew NaCl and $NaCl_{0.94}Br_{0.06}$ on GaAs (100) at 300 and 420 K. They found that NaCl grew epitaxially at 420 K but became a polycrystalline

film at 300 K. They believed that the epitaxial growth of alkali halides on semiconductors required a better lattice match, and the difference of thermal expansion coefficients partially accounts for the results.

In 1999, Kiguchi et al.[151] used MBE to grow KCl on KBr (001), with a lattice mismatch of 4.7%. They introduced extended X-ray absorption fine structure (EXAFS) to analyze the result. They found that with the increase of thickness of film, the K–Cl distance (parallel to substrate) increased and became close to the bulk KCl value when the film was thick enough. What is more is that they also found that the distance of K–Cl was rather close to the lattice constant of bulk KCl rather than that of KBr, even when the film was very thin. Later, Kiguchi et al.[152] used PVD to grow KCl/KBr (001), KCl/NaBr (001), NaCl/NaBr (001), KBr/KCl (001), and NaBr/KCl (001) thin films, though with a lattice mismatch of −4.6%, 5.6%, −5.6%, 4.9%, and −5.3%, respectively. Very recently, Chen et al.[153] used PVD to grow NaCl on NaCl (001). The homoepitaxy was analyzed and confirmed with *in situ* RHEED, scanning electron microscopy (SEM) and atomic force microscopy (AFM). Different substrate temperatures were attempted: 153, 298, and 393 K.

B. Wurtzite structure

1. Epitaxy on metals

The study on the epitaxy of wurtizte metal halides is uncommon, simply due to the scarcity of metal halides with the wurztite phase. In 1995, Skfrhn et al.[154] used CVD to grow β-AgI on Ag (001), (011), and (111). The substrate temperature was 353 and 473 K. Transmission electron microscopy (TEM) and selected area electron diffraction (SAED) were used to analyze the structure of the thin film. The epitaxial relation was revealed as AgI (0001)‖Ag (001) and AgI [11$\bar{2}$0]‖Ag [100], AgI (0001)‖Ag (001) and AgI [10$\bar{1}$0]‖Ag [100], and AgI (0001)‖Ag (001) and AgI [10$\bar{1}$0]‖Ag [110], respectively, and the lattice mismatches are 2.8%, 2.8%, and 3.2%, respectively.

2. Epitaxy on semiconductors/insulators

In 1970, Cochrane[155] used CVD to grow β-AgI thin films on mica and glass. The temperature of the substrate was at 313 K. Epitaxy was found between AgI and mica. Meanwhile, Brady et al.[156] used PVD to grow AgCl, AgBr, and AgI films on NaCl and mica. The substrate temperature for epitaxial AgI was between 373 and 423 K, while AgCl and AgBr can be epitaxially grown in a wider range of temperature. With TEM, the epitaxial relations were found to be: AgCl (111)‖mica (0001), AgCl (200)‖NaCl (001), AgBr (111)‖mica (0001), AgBr (200)‖NaCl (001), β-AgI (0001)‖mica (0001) and α/γ-AgI (111)‖mica (0001), β-AgI (0001)‖NaCl (200), and α/γ-AgI (111)‖NaCl (200), respectively.

C. Fluorite structure

1. Epitaxy on metals

Study on the epitaxy of fluorite structure metal halides has been mainly focused on CaF_2 which has been widely used as a buffer layer for the further epitaxial growth. In 2016, Chen et al.[157] used PVD to grow epitaxial CaF_2 as a buffer layer between Ni (001) and Ge (001). First, CaF_2 was deposited on Ni (001), at a substrate temperature of 623 K, with an epitaxial relation of CaF_2 [110]‖Ni [100] and CaF_2 [$\bar{1}$10]‖Ni [010]. Second, Ge (001) was epitaxially deposited to CaF_2 at 673 K, with a lattice mismatch of 3.2%. They found that Ge had a similar grain size with Ni.

2. Epitaxy on III–V substrates

In 1989, Maruo et al.[158,159] used MBE to grow CaF_2 on GaAs (001). They found that at 853 K, CaF_2 dissociated, but it grew as islands at 693 K. They showed that Ca grew on the top layer first and then CaF_2 was formed. In 1991, Colbow et al.[160] applied PVD to grow CaF_2 on GaAs (100). They found that at 823 K a monolayer of CaF_2 was grown. Meanwhile, Waho et al.[161] used MBE to grow (CaSr)F_2 ($Ca_{0.55}Sr_{0.45}F_2$) on GaAs (111). The substrate temperature was reduced from 973 to 723 K after a few monolayers had been grown. The mismatch at 723 K was 0. In addition, Engelhardt et al.[162] used MBE to grow $Ca_{0.43}Sr_{0.57}F_2$ on GaAs (100). The substrate temperature was 598 K. Synchrotron radiation photoemission and RHEED were introduced to analyze the results. They found that $Ca_{0.43}Sr_{0.57}F_2$ grew into an epitaxial island. In 1994, Santiago et al.[163] used PVD to grow BaF_2 on GaAs (100), (111), and (011). The substrate temperature was from 773 to 973 K. With X-ray photoelectron spectroscopy (XPS) and RHEED, they proved the successful epitaxial growth. In 1992, Weiss et al.[164] used MBE to grow CaF_2 and SrF_2 on InP (001). The substrate temperature was at 650 K. The epitaxy relation was revealed as: CaF_2 (001)‖InP (001). Based on LEED and AFM, they found that the surfaces were rough and contained 4-fold pyramids.

3. Epitaxy on IV-group substrates

In 2001, Sokolov et al.[165] used MBE to grow CaF_2 and CdF_2 on Si (111). They found the epitaxial relations as: CaF_2 (111)‖Si (111) and CaF_2 [1$\bar{1}$0]‖Si [1$\bar{1}$0], CaF_2 (001)‖Si (111), CdF_2 (111)‖Si (111), and CdF_2 [1$\bar{1}$0]‖Si [1$\bar{1}$0], CdF_2 (001)‖Si (111), respectively. On Si (001), CaF_2 grew as dots at a low temperature, while at high temperature it grew into wires (Fig. 8). In 1990, Tiwar et al.[166] used MBE to grow CdTe (100)/BaF_2 (100)/CaF_2 (100)/Si (100). The substrate temperature was 823 K for CaF_2 growth, and CaF_2 (100) and Si (100) showed a lattice mismatch of 0.6%. To grow BaF_2, the substrate temperature was first set

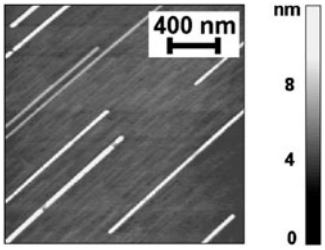

FIG. 8. CaF_2 nanowires grown on Si (111) at 700 °C. Reproduced with permission from Ref. 165.

at 823 K and then annealed at 973 K. For growth of CdTe, the substrate temperature was 473–623 K, and CdTe (100) and BaF_2 (100) showed a lattice mismatch of 4.5%. RHEED was used to analyze the structure and indicated good crystallinity in the CdTe film.

4. Epitaxy on metal halides

Bujor et al.[167] used PVD to grow CaF_2 on NaCl (100). They found that at 623 K, epitaxy was observed with CaF_2 (100)||NaCl (100) and CaF_2 ⟨110⟩||NaCl ⟨100⟩; at 473 K, the epitaxy was revealed as: CaF_2 (110)||NaCl (100) and CaF_2 ⟨111⟩||NaCl ⟨100⟩. These epitaxy results were successfully explained with a hard-sphere model.

D. Zincblende structure

1. Epitaxy on III–V compounds

Metal halide with zincblende structure is not populous.[168] Typical ones are copper-based. In 1992, Chen et al.[169] successfully applied PVD to grow epitaxial CuCl (110) on GaP (110). The substrate temperature was 373 K and the lattice mismatch was 0.8%. Later, Wake et al.[170] used PVD to grow CuX (X = Cl, Br, I) on GaAs (111) and GaAs (110). They found that when an interface had only covalent bonds, to realize epitaxy growth, a rigid lattice match relation between the substrate and film was required. Surface reconstructions occurred to relax the strain because of strong and directional features of covalent bonds. When an interface had only ionic bonds, however, it was found that epitaxy growth could be achieved even with a large lattice mismatch. The Phillips's ionicity of CuX is 0.692–0.746, which Cu-X bonds have both covalent and ionic characters. It was found that CuX was reconstructed to replicate the GaAs surface structure, and an epitaxy growth was achieved though the lattice mismatch between film and substrate is large.

2. Epitaxy on oxide substrates

In 1990s, Yanase et al.[171–174] used MBE to grow CuCl on MgO (001). The substrate temperature was between 333 and 353 K. The orientation relationships were CuCl (111)||MgO (001) and CuCl $[\bar{1}10]$||MgO [110]. It was found that CuCl on MgO (001) first formed triangular islands and then became hexagonal-shaped islands (Fig. 9). They attributed this kind of growth to the rapid diffusion of CuCl on MgO (001) because of excessive CuCl. At the same time, Wu et al.[175] achieved the epitaxial growth of the CuCl film on TiO_2 (110) via PVD with the substrate at room temperature.

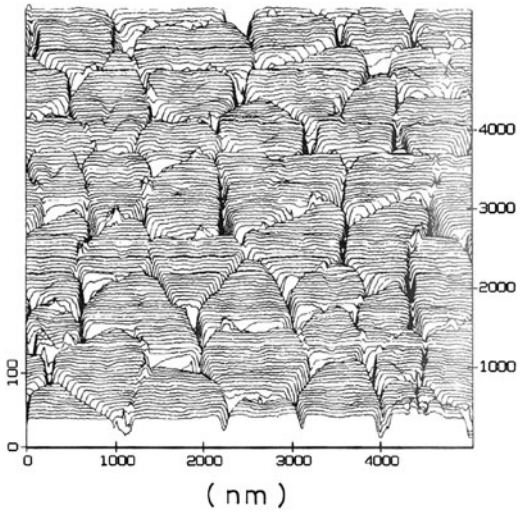

FIG. 9. AFM image of CuCl film grown on MgO (001). Reproduced with permission from Ref. 171.

E. Layered structure

1. Epitaxy on layered-structure substrates

Often to grow layered metal halides, substrates with a layered structure are preferred[176–178] (Fig. 10). In 1987, Nagamune et al.[179] attempted the epitaxial growth of PbI_2 on CdI_2 (001). The substrate temperature was 348–393 K. The lattice mismatch was 7.8% between CdI_2 and PbI_2. They attributed the successful epitaxial growth to weak van der Waals interaction. In 1990s, many studies were carried to epitaxially grow layered metal halides on layered substrates. Ueno et al.[180] used MBE to grow layered metal halides (PbI_2, CdI_2) on different kinds of layered substrates including MoS_2 (0001), $MoSe_2$ (0001), $NbSe_2$ (0001), $TaSe_2$ (0001), GaSe (0001), and Se-GaAs $(\bar{1}\bar{1}\bar{1})$. RHEED was introduced to analyze structures of thin films. Substrate temperature was at 150 °C. They concentrated on the growth of PbI_2 and found the epitaxial relations as: PbI_2 (0001)||MoS_2 (0001) and PbI_2 $[2\bar{1}\bar{1}0]$||MoS_2 $[10\bar{1}0]$, PbI_2 (0001)||$MoSe_2$ (0001) and PbI_2 $[2\bar{1}\bar{1}0]$||$MoSe_2$ $[10\bar{1}0]$ or $MoSe_2$ $[2\bar{1}\bar{1}0]$, PbI_2 (0001)||$NbSe_2$ (0001) and PbI_2 $[2\bar{1}\bar{1}0]$||$NbSe_2$ $[2\bar{1}\bar{1}0]$ with 19° offset, PbI_2 (0001)||$TaSe_2$ (0001)

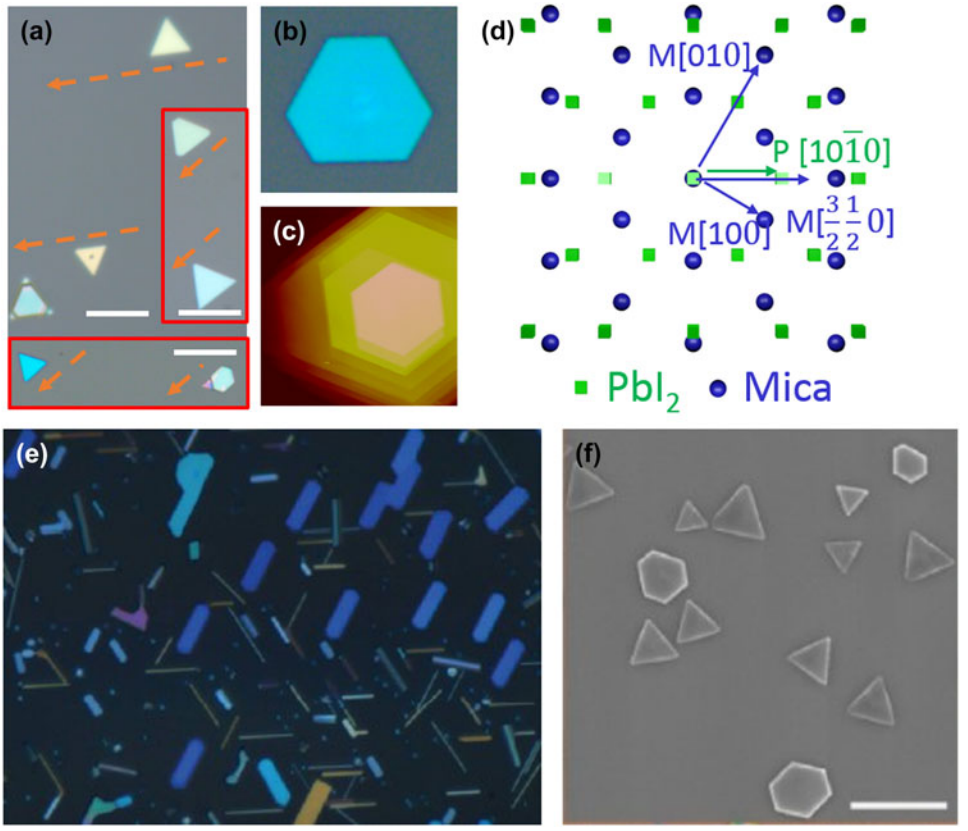

FIG. 10. (a–e) PbI_2 flakes grown on mica. (f) CdI_2 flakes on SiO_2. Reproduced with permission from Refs. 176, 178, and 182.

and PbI_2 [2$\bar{1}\bar{1}$0]||$TaSe_2$ [2$\bar{1}\bar{1}$0] with 19° offset, PbI_2 (0001)||GaSe (0001) and PbI_2 [2$\bar{1}\bar{1}$0]||GaSe [2$\bar{1}\bar{1}$0], and PbI_2 (0001)||GaSe (0001) and PbI_2 [2$\bar{1}\bar{1}$0]||GaSe [2$\bar{1}\bar{1}$0], despite large lattice mismatches of 44%, 38%, 32%, 31%, 21%, and 14%, respectively. Meanwhile, Kurisu et al.[181] achieved the epitaxial growth of PbI_2–CdI_2 superlattices on mica and/or sapphire. Recently, Wang et al.[182] applied CVD to grow PbI_2 flakes on mica [Figs. 10(a)–10(d)]. The substrate temperature was 523–573 K. The epitaxial relation was proposed to be PbI_2 [0001]||mica [001] with 5° offset and PbI_2 [10$\bar{1}$0]||mica [310].

In addition to CdI_2 and PbI_2, in 1990, Takeyama et al.[183] used a hot wall method to grow BiI_3 on PbI_2 (001) and CdI_2 (001) substrate. The substrate temperature was 293 K–363 K, respectively. Epitaxy was achieved though large in-plane lattice mismatches that existed, BiI_3 on PbI_2 (001): 39% and BiI_3 on CdI_2 (001): 43%.

2. Epitaxy on III–V compounds

In 1990, Mowbray et al.[184] achieved the epitaxial growth of CdI_2 on InSb (001) via PVD with the substrate temperature at 310 K. The epitaxial relation was found as CdI_2 (0001)||InSb (001).

F. CsCl structure

1. Epitaxy on oxide substrates

For the CsCl structure, the metal halide is mainly focused on Cs-based compounds. In 1999, Suzuki et al.[185] realized the epitaxial growth of CsCl on MgO (001) by PVD. The substrate was gradually heated from 293 to 673 K. The epitaxial relations were (001) α-CsCl||(001) MgO & [100] α-CsCl||[100] MgO, (001) β-CsCl||(001) MgO & [110] β-CsCl||[100] MgO. The lattice mismatch between α-CsCl and MgO is 2.1%.

2. Epitaxy on metal halides

Common substrates for CsCl-type metal halide film growth are metal halides themselves. In 2003, Yoshikawa et al.[186] used MBE to grow CsCl on GaAs (001). At 470 K, the epitaxial relation was found as CsCl (001)||GaAs (001) and [100] CsCl||[100] GaAs. At the same time, Kiguchi et al.[187] applied MBE to grow CsBr on LiF (001) and KBr (001). They found that, on LiF (001), at 300 K, α-CsCl was formed and had an epitaxial relation of (110) α-CsBr||(001) LiF and [001] α-CsBr||[001] LiF. At 400 K, β-CsCl was formed and had an epitaxial relation of (001) β-CsBr||(001) LiF and [100]

β-CsBr||[100] LiF. On KBr (001), however, at 300–500 K, only β-CsCl was observed with an epitaxial relation of (001) β-CsBr||(001) KBr and [100] β-CsBr||[100] KBr.

G. Perovskite structure

1. Epitaxy on layered substrates

Most studies on the vapor phase epitaxy of metal halide perovskites were carried very recently and the substrate was focused on layered materials. In 2015, Wang et al.[188] applied CVD to grow $MAPbCl_3$ films (MA– = CH_3NH_3–) on mica [Figs. 11(a)–11(d) and 11(g)–11(i)]. TEM and AFM were used to analyze the structure of films. The epitaxy relation was found as mica (001)||$MAPbCl_3$ (001), mica (200)||$MAPbCl_3$ (200) (with 5° offset), and mica (020)||perovskite (010) (with 5° offset). They also developed a new model to analyze the kinetics in van der Waals epitaxy. With this model, they explained the 2D-layered growth of 3D-structured $MAPbCl_3$, combined with a Monte Carlo simulation. In 2016, Zhang et al.[189] used a same CVD method and successfully grew high-quality epitaxial $CsPbX_3$ sheets (X = Cl, Br, I) on muscovite mica [Figs. 11(e)–11(f)].

In addition to nanosheets, the nanowire morphology epitaxially grown on certain substrates was also realized recently. In 2016, Wang et al.[190] used CVD to grow $CsPbX_3$ (X = Br, I) nanowires on mica with the substrate temperature at 673 K [Figs. 12(a)–12(c)]. A large scale of aligned nanowires with 3-fold in-plane symmetry was observed. The epitaxial relation was $CsPbX_3$ (011)||mica (001) and $CsPbX_3$ (100)||mica (020) with a 30° offset. Almost at the same time, Chen et al.[191] applied a similar method for the growth of $CsPbX_3$ (X = Cl, Br, I) nanowires on mica and found the same epitaxial relations [Fig. 12(d)]. Besides the inorganic halide perovskites, their hybrid counterparts have also been achieved epitaxially. In 2017, Wang et al.[192] demonstrated the growth of $MAPbI_3$/$MAPbBr_3$ nanowires double heterojunction on mica by vapor phase epitaxy [Figs. 12(e) and 12(f)]. It was found

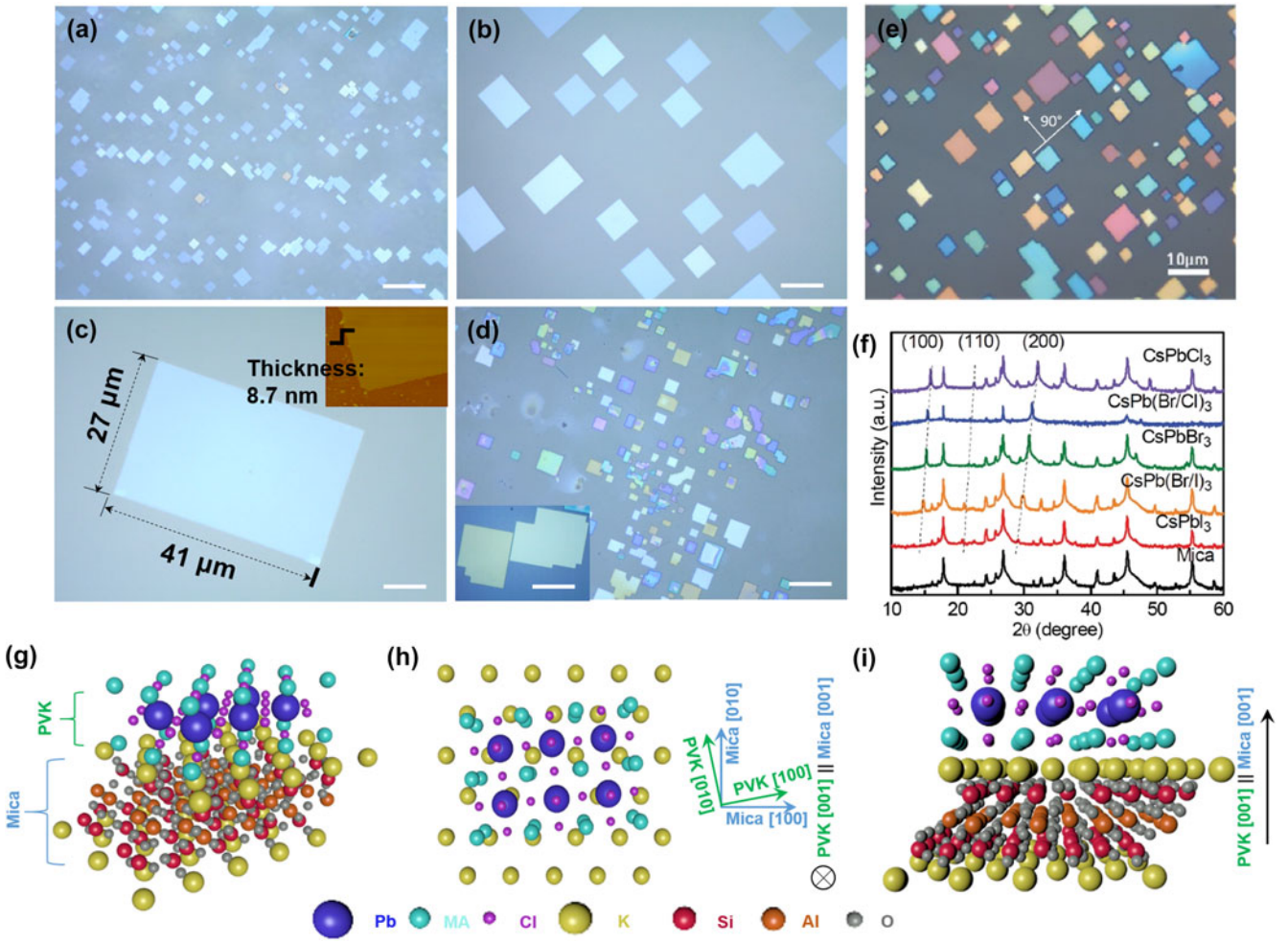

FIG. 11. (a–d) Hybrid perovskite sheets grown on mica. (e, f) Inorganic perovskite sheets on mica. (g–i) Epitaxial model between perovskite and mica. Reproduced with permission from Refs. 188 and 189.

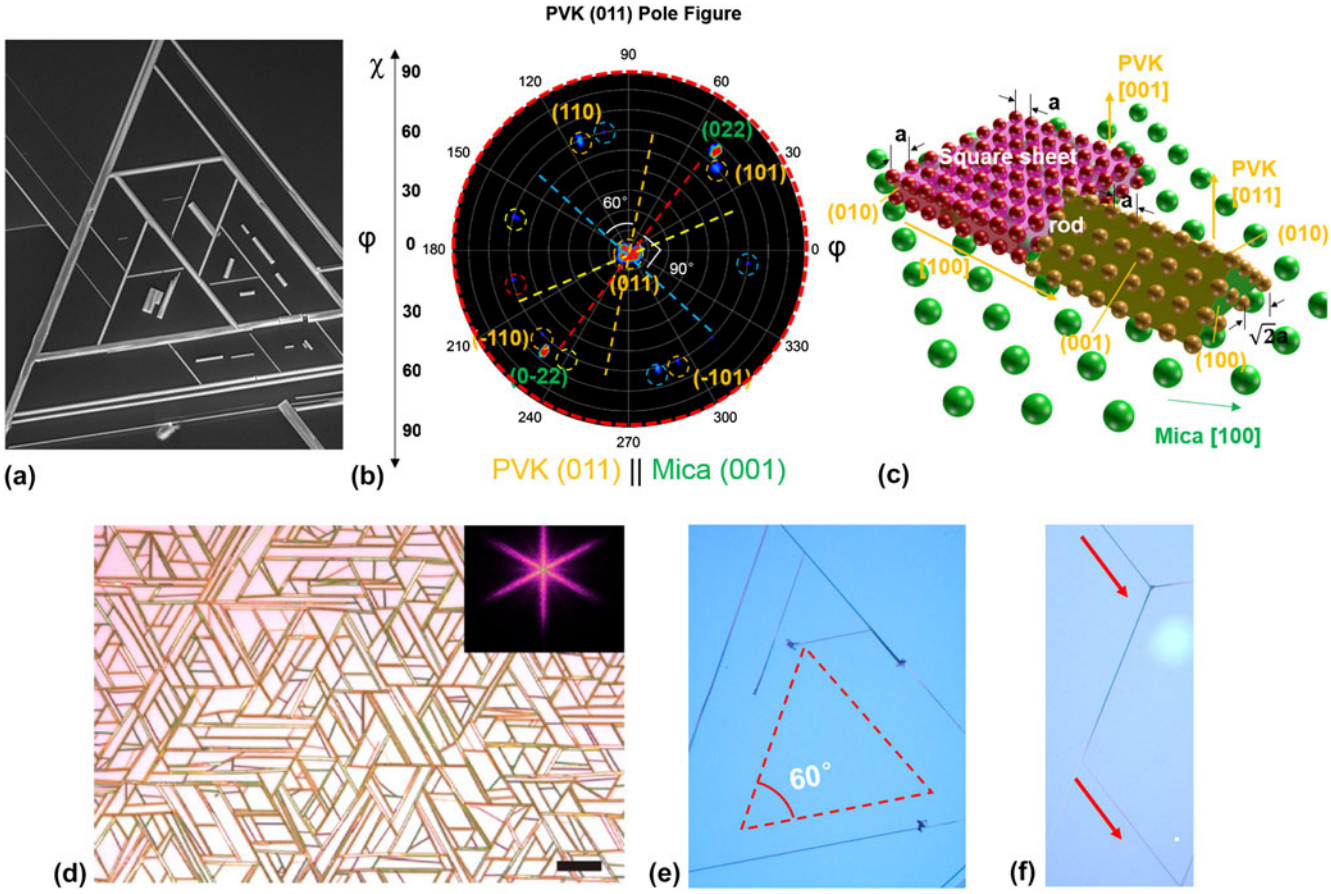

FIG. 12. Perovskite halide nanowires on mica. (a–d) Inorganic perovskite. (e, f) Hybrid perovskite. Reproduced with permission from Refs. 190, 191, and 192.

that the growth temperature for the hybrid system was slightly lower than their pure inorganic systems.

IV. SUMMARY

In summary, this review comprehensively covers the major physical properties of general metal halide materials: photodecomposition, ionic conducting, ferroelectricity, Rashba splitting, magnetic properties, optoelectronic/electro-optic properties, electron beam-induced decomposition, superconductivity, chemical adsorption-induced electrical conductivity modification, and radiation-induced electrical conductivity change. It also thoroughly covers the major progresses in the vapor phase epitaxial growth of metal halide materials with CsCl structure, fluorite, layered, zinc-blende, wurtzite, rocksalt, and perovskites. In the vapor phase epitaxy, important parameters/growth results such as substrate temperatures, epitaxial relations, substrate selections, and growth morphologies are discussed. It is our hope that this review could be helpful in inspiring the discovery of new properties or designing growth parameters for emerging metal halide crystals.

ACKNOWLEDGMENTS

Y.H., Y.W., Z.C., E.W., and J.S. are supported by NSF Awards under CMMI 1550941 and CMMI 1635520. X.S. is supported by the NYSTAR Focus Center at RPI, C130117.

REFERENCES

1. W. Zhang, G.E. Eperon, and H.J. Snaith: Metal halide perovskites for energy applications. *Nat. Energy* **1**, 16048 (2016).
2. S.D. Stranks and H.J. Snaith: Metal-halide perovskites for photovoltaic and light-emitting devices. *Nat. Nanotechnol.* **10**, 391–402 (2015).
3. Y.J. Fang, Q.F. Dong, Y.C. Shao, Y.B. Yuan, and J.S. Huang: Highly narrowband perovskite single-crystal photodetectors enabled by surface-charge recombination. *Nat. Photonics* **9**, 679–686 (2015).
4. H.M. Zhu, Y.P. Fu, F. Meng, X.X. Wu, Z.Z. Gong, Q. Ding, M.V. Gustafsson, M.T. Trinh, S. Jin, and X.Y. Zhu: Lead halide perovskite nanowire lasers with low lasing thresholds and high quality factors. *Nat. Mater.* **14**, 636–642 (2015).
5. Q.F. Dong, Y.J. Fang, Y.C. Shao, P. Mulligan, J. Qiu, L. Cao, and J.S. Huang: Electron-hole diffusion lengths >175 μm in solution-grown $CH_3NH_3PbI_3$ single crystals. *Science* **347**, 967–970 (2015).
6. S.D. Stranks, G.E. Eperon, G. Grancini, C. Menelaou, M.J.P. Alcocer, T. Leijtens, L.M. Herz, A. Petrozza, and H.J. Snaith: Electron-hole diffusion lengths exceeding 1

micrometer in an organometal trihalide perovskite absorber. *Science* **342**, 341–344 (2013).
7. Z.Z. Chen, Y.P. Wang, Y.H. Shi, B. Hsu, Z. Yang, and J. Shi: Regulating carrier dynamics in single crystal halide perovskite via interface engineering and optical doping. *Adv. Electron. Mater.* **2**, 1600248–1600254 (2016).
8. W.Q. Liao, Y. Zhang, C.L. Hu, J.G. Mao, H.Y. Ye, P.F. Li, S.D. Huang, and R.G. Xiong: A lead-halide perovskite molecular ferroelectric semiconductor. *Nat. Commun.* **6**, 7338 (2015).
9. A. Stroppa, D. Di Sante, P. Barone, M. Bokdam, G. Kresse, C. Franchini, M.H. Whangbo, and S. Picozzi: Tunable ferroelectric polarization and its interplay with spin-orbit coupling in tin iodide perovskites. *Nat. Commun.* **5**, 5900 (2014).
10. A. Crepaldi, L. Moreschini, G. Autes, C. Tournier-Colletta, S. Moser, N. Virk, H. Berger, P. Bugnon, Y.J. Chang, K. Kern, A. Bostwick, E. Rotenberg, O.V. Yazyev, and M. Grioni: Giant ambipolar Rashba effect in the semiconductor BiTeI. *Phys. Rev. Lett.* **109**, 096803 (2012).
11. C. Felser, K. Ahn, R.K. Kremer, R. Seshadri, and A. Simon: Giant negative magnetoresistance in GdI_2—Prediction and realization. *J. Solid State Chem.* **147**, 19–25 (1999).
12. S.V. Eremeeva, I.A. Nechaev, and E.V. Chulkov: Giant Rashba type spin splitting at polar surfaces of BiTeI. *JETP Lett.* **96**, 437–444 (2012).
13. K. Ishizaka, M.S. Bahramy, H. Murakawa, M. Sakano, T. Shimojima, T. Sonobe, K. Koizumi, S. Shin, H. Miyahara, A. Kimura, K. Miyamoto, T. Okuda, H. Namatame, M. Taniguchi, R. Arita, N. Nagaosa, K. Kobayashi, Y. Murakami, R. Kumai, Y. Kaneko, Y. Onose, and Y. Tokura: Giant Rashba-type spin splitting in bulk BiTeI. *Nat. Mater.* **10**, 521–526 (2011).
14. B. Huang, G. Clark, E. Navarro-Moratalla, D.R. Klein, R. Cheng, K.L. Seyler, D. Zhong, E. Schmidgall, M.A. McGuire, D.H. Cobden, W. Yao, D. Xiao, P. Jarillo-Herrero, and X. Xu: Layer-dependent ferromagnetism in a van der Waals crystal down to the monolayer limit. *Nature* **546**, 270–273 (2017).
15. C. Huang, J. Zhou, H. Wu, K. Deng, P. Jena, and E. Kan: Quantum anomalous Hall effect in ferromagnetic transition metal halides. *Phys. Rev. B* **95**, 045113 (2017).
16. G.E. Eperon, G.M. Paterno, R.J. Sutton, A. Zampetti, A.A. Haghighirad, F. Cacialli, and H.J. Snaith: Inorganic caesium lead iodide perovskite solar cells. *J. Mater. Chem. A* **3**, 19688–19695 (2015).
17. H.M. Zhu, K. Miyata, Y.P. Fu, J. Wang, P.P. Joshi, D. Niesner, K.W. Williams, S. Jin, and X.Y. Zhu: Screening in crystalline liquids protects energetic carriers in hybrid perovskites. *Science* **353**, 1409–1413 (2016).
18. Z.N. Song, S.C. Watthage, A.B. Phillips, B.L. Tompkins, R.J. Ellingson, and M.J. Heben: Impact of processing temperature and composition on the formation of methylammonium lead iodide perovskites. *Chem. Mater.* **27**, 4612–4619 (2015).
19. R. Kanno, Y. Takeda, Y. Masuyama, O. Yamamoto, and T. Takahashi: Phase-diagram high copper–ion conductivity of the copper (I) chloride rubidium chloride system. *Solid State Ionics* **11**, 221–226 (1983).
20. M.R. Tubbs: The optical properties and chemical decomposition of halides with layer structures II. Defects, chemical decomposition, and photographic phenomena. *Phys. Status Solidi* **67**, 11–49 (1975).
21. M.R. Tubbs: The optical properties and chemical decomposition of lead iodide. *Proc. R. Soc., Ser. A* **280**, 566–585 (1964).
22. R.I. Dawood, A.J. Forty, and M.R. Tubbs: The photodecomposition of lead iodide. *Proc. R. Soc., Ser. A* **284**, 272–288 (1964).
23. A. Kaldor and G.A. Somorjai: Photodecomposition of lead chloride. *J. Phys. Chem.* **70**, 3538–3544 (1966).
24. H.E. Spencer and J.O. Darlak: Lead bromide photochemistry: Reduction of lead ion and oxidation of leucocrystal violet. *J. Phys. Chem.* **72**, 2384–2389 (1968).
25. R.A. Fotland: Photoconductivity and photolysis in cadmium iodide. *J. Phys. Chem.* **33**, 956 (1960).
26. M.R. Tubbs: High resolution image recording on phtosensitive halide layers. *J. Photogr. Sci.* **17**, 162–169 (1969).
27. F. Moser, N.R. Nail, and F. Urbach: Optical absorption studies of the volume photolysis of large silver chloride crystals. *J. Phys. Chem. Solids* **9**, 217–234 (1959).
28. R.W. Gurney and N.F. Mott: The theory of the photolysis of silver bromide and the photographic latent image. *Proc. R. Soc., Ser. A* **164**, 151–167 (1938).
29. F.C. Brown: Electronic properties and band structure of the silver halides. *J. Phys. Chem.* **66**, 2368–2376 (1962).
30. W. West and V.I. Saunders: Photochemical processes in thin single crystals of silver bromide: The distribution and behavior of latent image and photolytic silver in pure crystals and in crystals containing foreign cation. *J. Phys. Chem.* **63**, 45–54 (1959).
31. S. Xu, H. Zhou, J. Xu, and Y. Li: Synthesis of size-tunable silver iodide nanowires in reverse micelles. *Langmuir* **18**, 10503–10504 (2002).
32. J.F. Verwey: The photolysis of lead chloride and lead bromide. *J. Phys. Chem. Solids* **27**, 468–474 (1965).
33. S.E. Sheppard and W. Vanselow: The lattice energies of the silver halides and their photochemical decomposition. II. *J. Phys. Chem.* **34**, 2719–2748 (1930).
34. A. Muray, M. Isaacson, and I. Adesida: AlF3—A new very high resolution electron beam resist. *Appl. Phys. Lett.* **45**, 589 (1984).
35. M.W. Geis, J.N. Randall, T.F. Deutsch, P.D. DeGraff, K.E. Krohn, and L.A. Stern: Self-developing resist with submicrometer resolution and processing stability. *Appl. Phys. Lett.* **43**, 74 (1983).
36. W. Langheinrich, B. Spangenberg, and H. Beneking: Nanostructure fabrication using lithium fluoride films as an electron beam resist. *J. Vac. Sci. Technol., B: Microelectron. Nanometer Struct.–Process., Meas., Phenom.* **10**, 2868 (1992).
37. E. Kratschmer and M. Isaacson: Progress in self-developing metal fluoride resists. *J. Vac. Sci. Technol., B: Microelectron. Process. Phenom.* **5**, 369 (1987).
38. A. Muray, M. Scheinfein, and M. Isaacson: Radiolysis and resolution limits of inorganic halide resists. *J. Vac. Sci. Technol., B: Microelectron. Process. Phenom.* **3**, 367 (1985).
39. G. Kuwabara and K. Aoyagi: Photoconductivity of some alkali halide crystals in the functional absorption range. *J. Phys. Chem. Solids* **22**, 333–338 (1961).
40. B.L. Evans: Optical property of animony triiodide. *Proc. R. Soc., Ser. A* **276**, 136–148 (1963).
41. I. Lefkowitz, R.P. Lowndes, and A.D. Yoffe: Direct observation of excitons in some thallous halide single crystals. *J. Phys. Chem. Solids* **26**, 1171–1175 (1965).
42. G. Baldini and B. Bosacchi: Optical properties of alkali-halide crystals. *Phys. Rev.* **166**, 3 (1968).
43. O.L. Hsu and C.W. Bates, Jr.: Excitonic emission from CsI (Na). *Phys. Rev. B* **15**, 12 (1977).
44. J.I. Larruquert, J.A. Méndez, J.A. Aznárez, A.S. Tremsin, and O.H.W. Siegmund: Optical properties and quantum efficiency of thin-film alkali halides in the far ultraviolet. *Appl. Opt.* **41**, 13 (2002).
45. L.W. Campbell and F. Gao: Excited state electronic properties of sodium iodide and cesium iodide. *J. Lumin.* **137**, 121–131 (2013).
46. T. Komatsu, Y. Kaifu, T. Karasawa, and T. Iidoa: Stacking fault and surface effects on exciton spectra in layered metal halides. *Physica B+C* **99**, 318–322 (1980).

47. Y. Nakai and K. Teegarden: Phtoconductivity in RbI and KI. *J. Phys. Chem. Solids* **22**, 327–331 (1961).
48. R.F. Wood: The relaxed exciton in alkali halide crystal. *Solid State Commun.* **4**, 39–42 (1965).
49. J.F. Dillon, Jr., H. Kamimura, and J.P. Remeika: Magneto-optical properties of ferromagnetic chromium trihalides. *J. Phys. Chem. Solids* **27**, 1531–1549 (1966).
50. K. Ahn, R.K. Kremer, and A. Simon: Effect of geometrical frustration on the magnetic properties of the triangular-layer system $Tb_2C_2I_2$: A neutron diffraction investigation. *J. Phys.: Condens. Matter* **16**, 11 (2004).
51. A. Kasten, P.H. Moller, and M. Schienle: Magnetic ordering in GdI_2. *Solid State Commun.* **51**, 919–921 (1984).
52. R.I. Joseph and E. Schlömann: Demagnetizing field in non-ellipsoidal bodies. *J. Appl. Phys.* **36**, 1579 (1965).
53. Y. Zhou, H. Lu, X. Zu, and F. Gao: Evidencing the existence of exciting half-metallicity in two-dimensional $TiCl_3$ and VCl_3 sheets. *Sci. Rep.* **6**, 19407 (2016).
54. P. Lauque, M. Bendahan, J-L. Seguin, M. Pasquinelli, and P. Knauth: Electrical properties of thin-films of the mixed ionic-electronic conductor CuBr—Influence of electrode metals and gaseous ammonia. *J. Eur. Ceram. Soc.* **19**, 823–826 (1999).
55. P. Lauque, M. Bendahan, J-L. Seguin, K.A. Ngo, and P. Knauth: Highly sensitive and selective room temperature NH_3 gas micro-sensor using an ionic conductor CuBr film. *Anal. Chim. Acta* **515**, 279–284 (2004).
56. U. Lauer, J. Maier, and W. Gopel: Conductance effects of ammonia on silver chloride boundary layers. *Sens. Actuators, B* **2**, 125–131 (1990).
57. N. Rao, C.M.v.d. Bleek, J. Schoonman, and O.T. Sorensen: A novel temperature-gradient Na-b-alumina solid. *Solid State Ionics* **53–56**, 30–38 (1992).
58. H. Ichida, M. Nakayama, and H. Nishimura: Stimulated emission from exciton–exciton scattering in CuBr thin films. *J. Lumin.* **87–89**, 235–237 (2000).
59. J-L. Seguin, M. Bendahan, G. Lollmun, M. Pasquinelli, and P. Knauth: Preparation of thin films of copper (I) bromide by r.f. sputtering: Morphology and electrical properties. *Thin Solid Films* **323**, 31–36 (1998).
60. J-L. Seguin, M. Bendahan, P. Lauque, C. Jacolin, M. Pasquinelli, and P. Knauth: Mixed ionic-electronic conducting thin-films of CuBr a new active component for gas sensors. *Sens. Actuators, A* **74**, 237–241 (1999).
61. J. Maier and U. Lauer: Ionic contact equilibria in solids—Implications for batteries and sensors. *Ber. Bunsen-Ges. Phys. Chem.* **94**, 973–978 (1990).
62. J. Maier: Ionic conduction in space charge regions. *Prog. Solid State Chem.* **23**, 171–236 (1995).
63. P. Lauque, J-M. Laugier, C. Jacolin, M. Bendahan, C. Lemire, and P. Knauth: Impedance analysis of CuBr films for ammonia gas detection. *Sens. Actuators, B* **87**, 431–436 (2002).
64. P. Lauque, M. Bendahan, C. Jacolin, J-L. Seguin, M. Pasquinelli, and P. Knauth: Electrical properties and sensor characteristics for NH_3 gas of sputtered CuBr films. *Sens. Actuators, B* **59**, 216–219 (1999).
65. J. Maier: Electrical sensing of complex gaseous species by making use of acid-base properties. *Solid State Ionics* **62**, 105–111 (1993).
66. J. Coetzer: A new high energy density battery system. *J. Power Sources* **18**, 377–380 (1986).
67. R. Benato, N. Cosciani, G. Crugnola, S.D. Sessa, G. Lodi, C. Parmeggiani, and M. Todeschini: Sodium nickel chloride battery technology for large-scale stationary storage in the high voltage network. *J. Power Sources* **293**, 127–136 (2015).
68. G. Li, X. Lu, J.Y. Kim, J.P. Lemmon, and V.L. Sprenkle: Improved cycling behavior of ZEBRA battery operated at intermediate temperature of 175 °C. *J. Power Sources* **249**, 414–417 (2014).
69. R.J. Bones, J. Coetzer, R.C. Galloway, and D.A. Teagle: A sodium: Iron (II) chloride cell with a beta alumina electrolyte. *J. Electrochem. Soc.* **134**, 2379–2382 (1987).
70. C.J. Brabec, S.E. Shaheen, C. Winder, and N.S.S. Denk: Effect of LiF metal electrodes on the performance of plastic solar cells. *Appl. Phys. Lett.* **80**, 1288 (2002).
71. X. Lu, G. Xia, J.P. Lemmon, and Z. Yang: Advanced materials for sodium-beta alumina batteries—Status, challenges and perspectives. *J. Power Sources* **195**, 2431–2442 (2010).
72. K. Frutschy, T. Chatwin, and R. Bull: Cell overcharge testing inside sodium metal halide battery. *J. Power Sources* **291**, 117–125 (2015).
73. J. Prakash, L. Redey, and D.R. Vissers: Dynamic performance measurements of $Na/NiCl_2$ cells for electric vehicle applications. *J. Power Sources* **87**, 195–200 (2000).
74. L. Sanz, J. Palma, E. García-Quismondo, and M. Anderson: The effect of chloride ion complexation on reversibility and redox potential of the Cu (II):Cu (I) couple for use in redox flow batteries. *J. Power Sources* **224**, 278–284 (2013).
75. X. Lu, G. Li, J.Y. Kim, J.P. Lemmon, V.L. Sprenkle, and Z. Yang: The effects of temperature on the electrochemical performance of sodium–nickel chloride batteries. *J. Power Sources* **215**, 288–295 (2012).
76. E. Gerovasili, J.F. May, and D.U. Sauer: Experimental evaluation of the performance of the sodium metal chloride battery below usual operating temperatures. *J. Power Sources* **251**, 137–144 (2014).
77. X. Lu, J.P. Lemmon, J.Y. Kim, V.L. Sprenkle, and Z. Yang: High energy density $Na–S:NiCl_2$ hybrid battery. *J. Power Sources* **224**, 312–316 (2013).
78. M. Hosseinifar and A. Petric: High temperature versus low temperature Zebra ($Na:NiCl_2$) cell performance. *J. Power Sources* **206**, 402–408 (2012).
79. J. Rijssenbeeka, Y. Gao, Z. Zhong, M. Croftc, N. Jisrawi, A. Ignatov, and T. Tsakalakos: *In situ* X-ray diffraction of prototype sodium metal halide cells—Time and space electrochemical profiling. *J. Power Sources* **196**, 2332–2339 (2011).
80. S. Longo, V. Antonucci, M. Cellura, and M. Ferraro: Life cycle assessment of storage systems—The case study of a sodium: nickel chloride battery. *J. Cleaner Prod.* **85**, 337–346 (2014).
81. D. Eroglu and A.C. West: Modeling of reaction kinetics and transport in the positive porous electrode in a sodium–iron chloride battery. *J. Power Sources* **203**, 211–221 (2012).
82. A. van Zyl: Review of the Zebra battery system development. *Solid State Ionics* **86–88**, 883–889 (1996).
83. J.L. Sudworth: The sodim:nickle choloride (ZEBRA) battery. *J. Power Sources* **100**, 149–163 (2001).
84. M.E. Bowden, K.J. Alvine, J.L. Fulton, J.P. Lemmon, X. Lu, B-J. Webb-Robertson, S.M. Heald, M. Balasubramanian, D.R. Mortensen, G.T. Seidler, and N.J. Hess: X-ray absorption measurements on nickel cathode of sodium-beta alumina batteries—Fe–Ni–Cl chemical associations. *J. Power Sources* **247**, 517–526 (2014).
85. H. Bohm and G. Beyermann: ZEBRA batteries, enhanced power by doping. *J. Power Sources* **84**, 270–274 (1990).
86. R.C. Galloway and S. Haslam: The ZEBRA electric vehicle battery—Power and energy improvements. *J. Power Sources* **80**, 164–167 (1999).
87. R. Hofstardter: Alkali halide scintillation counters. *Phys. Rev.* **74**, 100 (1948).

88. B.D. Milbrath, A.J. Peurrung, M. Bliss, and W.J. Weber: Radiation detector materials—An overview. *J. Mater. Res.* **23**, 10 (2008).
89. S. Roth and W.R. Willig: Lead iodide nuclear particle detectors. *Appl. Phys. Lett.* **18**, 328 (1971).
90. E.V.D. van Loef, P. Dorenbos, C.W.E. van Eijk, K. Krämer, and H.U. Güdel: Scintillation properties of $LaCl_3$–Ce^{3+} crystals—Fast, efficient, and high-energy resolution scintillators. *IEEE Trans. Nucl. Sci.* **48**, 3 (2001).
91. K.S. Shah, J. Glodo, M. Klugerman, W.M. Higgins, T. Gupta, and P. Wong: High energy resolution scintillation spectrometers. *IEEE Trans. Nucl. Sci.* **51**, 5 (2004).
92. E.V.D. van Loef, P. Dorenbos, C.W.E. van Eijk, K. Krämer, and H.U. Güdel: High energy resolution scintillator—Cs^{3+} activated $LaBr_3$. *Appl. Phys. Lett.* **79**, 1573 (2001).
93. M.D. Birowosuto, P. Dorenbos, C.W.E. van Eijk, K. Krämer, and H.U. Güdel: High light output scintillator for photodiode readout—LuI_3:Ce^{3+}. *J. Appl. Phys.* **99**, 123520 (2006).
94. X. Chen, T. Koiwasaki, and S. Yamanaka: High-pressure synthesis and crystal structures of β-MNCl (M = Zr and Hf). *J. Solid State Chem.* **159**, 80–86 (2001).
95. S. Shamoto, K. Iizawa, T. Koiwasaki, M. Yasukawa, S. Yamanaka, O. Petrenko, S.M. Bennington, H. Yoshida, K. Ohoyama, Y. Yamaguchi, Y. Qno, Y. Miyazaki, and T. Kajitani: Pressure effect and neutron scattering study on AxHfNCl. *Physica C* **341–348**, 747–748 (2000).
96. R.K. Kremer and A. Simon: Superconductivity and magnetoresistance in unusual layered rare earth halides and rare earth carbides. *Curr. Appl. Phys.* **4**, 563–569 (2004).
97. J. Nagamatsu, N. Nakagawa, T. Muranaka, Y. Zenitani, and J. Akimitsu: Superconductivity at 39 K in magnesium diboride. *Nature* **410**, 63–64 (2001).
98. S. Yamanaka and H. Tou: Superconductivity in electron-doped layer-structured nitride halides. *Curr. Opin. Solid State Mater. Sci.* **5**, 545–551 (2001).
99. R.W. Henn, W. Schnelle, R.K. Kremer, and A. Simon: Bulk superconductivity at 10 K in the layered compounds $Y_2C_2I_2$ and $Y_2C_2Br_2$. *Phys. Rev. Lett.* **77**, 2 (1996).
100. S. Yamanaka, H. Kawaji, K-I. Hotehama, and M. Ohashi: A new layerstructured nitride superconductor. Lithium-intercalated 8-zirconium nitride chloride, Li_xZrNCl. *Adv. Mater.* **8**, 9 (1996).
101. S. Yamanaka, K-I. Hotehama, and H. Kawaji: Superconductivity at 25.5 K in electron-doped layered hafnium nitride. *Nature* **392**, 580–583 (1998).
102. Z.P. Yin and G. Kotliar: Rational material design of mixed-valent high-T_c superconductors. *EPL* **101**, 2 (2013).
103. H. Maass, H. Bentmann, C. Seibel, C. Tusche, S.V. Eremeev, T.R. Peixoto, O.E. Tereshchenko, K.A. Kokh, E.V. Chulkov, J. Kirschner, and F. Reinert: Spin-texture inversion in the giant Rashba semiconductor BiTeI. *Nat. Commun.* **7**, 11621 (2016).
104. M.S. Bahramy, R. Arita, and N. Nagaosa: Origin of giant bulk Rashba splitting—Application to BiTeI. *Phys. Rev. B* **84**, 041202 (2011).
105. G. Landolt, S.V. Eremeev, Y.M. Koroteev, B. Slomski, S. Muff, T. Neupert, M. Kobayashi, V.N. Strocov, T. Schmitt, Z.S. Aliev, M.B. Babanly, I.R. Amiraslanov, E.V. Chulkov, J. Osterwalder, and J.H. Dil: Disentanglement of surface and bulk Rashba spin splittings in noncentrosymmetric BiTeI. *Phys. Rev. Lett.* **109**, 116403 (2012).
106. J.S. Lee, G.A. Schober, M.S. Bahramy, H. Murakawa, Y. Onose, R. Arita, N. Nagaosa, and Y. Tokura: Optical response of relativistic electrons in the polar BiTeI semiconductor. *Phys. Rev. Lett.* **107**, 117401 (2011).
107. M.K. Tran, J. Levallois, P. Lerch, J. Teyssier, A.B. Kuzmenko, G. Autes, O.V. Yazyev, A. Ubaldini, E. Giannini, D. van der Marel, and A. Akrap: Infrared- and Raman-spectroscopy measurements of a transition in the crystal structure and a closing of the energy gap of BiTeI under pressure. *Phys. Rev. Lett.* **112**, 047402 (2014).
108. P. Tang, B. Yan, W. Cao, S-C. Wu, C. Felser, and W. Duan: Weak topological insulators induced by the interlayer coupling—A first-principles study of stacked Bi_2TeI. *Phys. Rev. B* **89**, 041409 (2014).
109. C.J. Butler, P.Y. Yang, R. Sankar, Y.N. Lien, C.I. Lu, L.Y. Chang, C.H. Chen, C.M. Wei, F.C. Chou, and M.T. Lin: Quasiparticle scattering in the Rashba semiconductor BiTeBr: The roles of spin and defect lattice site. *ACS Nano* **10**, 9361–9369 (2016).
110. G. Landolt, S.V. Eremeev, O.E. Tereshchenko, S. Muff, B. Slomski, K.A. Kokh, M. Kobayashi, T. Schmitt, V.N. Strocov, J. Osterwalder, E.V. Chulkov, and J.H. Dil: Bulk and surface Rashba splitting in single termination BiTeCl. *New J. Phys.* **15**, 085022 (2013).
111. Y.L. Chen, M. Kanou, Z.K. Liu, H.J. Zhang, J.A. Sobota, D. Leuenberger, S.K. Mo, B. Zhou, S-L. Yang, P.S. Kirchmann, D.H. Lu, R.G. Moore, Z. Hussain, Z.X. Shen, X.L. Qi, and T. Sasagawa: Discovery of a single topological Dirac fermion in the strong inversion asymmetric compound BiTeCl. *Nat. Phys.* **9**, 704–708 (2013).
112. S.V. Eremeev, I.P. Rusinov, I.A. Nechaev, and E.V. Chulkov: Rashba split surface states in BiTeBr. *New J. Phys.* **15**, 075015 (2013).
113. M. Kim, J. Im, A.J. Freeman, J. Ihm, and H. Jin: Switchable $S = 1/2$ and $J = 1/2$ Rashba bands in ferroelectric halide perovskites. *Proc. Natl. Acad. Sci. U. S. A.* **111**, 6900–6904 (2014).
114. E. Fatuzzo, G. Harbeke, W.J. Merz, R. Nitsche, H. Roetschi, and N. Ruppet: Ferroelectricity in SbSI. *Phys. Rev.* **127**, 6 (1962).
115. M. Zhang, S. Pan, Z. Yang, Y. Wang, X. Su, A.Y. Yang, Z. Huang, S. Han, and K.R. Poeppelmeier: BaClBF4—A new noncentrosymmetric pseudo-Aurivillius type material with transparency range from deep UV to middle IR and a high laser damage threshold. *J. Mater. Chem. C* **1**, 4740 (2013).
116. T. Kurumaji, S. Seki, S. Ishiwata, H. Murakawa, Y. Kaneko, and Y. Tokura: Magnetoelectric responses induced by domain rearrangement and spin structural change in triangular-lattice helimagnets NiI_2 and CoI_2. *Phys. Rev. B* **87**, 014429 (2013).
117. K.S. Aleksandrov, V.N. Voronov, A.N. Vtyurin, S.A. Goryainov, N.G. Zamkova, V.I. Zinenko, and A.S. Krylov: Pressure-induced phase transitions in ScF_3 crystal—Raman spectra and lattice dynamics. *Ferroelectrics* **284**, 31–45 (2003).
118. Q. Yang, K. Tang, C. Wang, J. Zuo, and Y. Qian: The synthesis and characterization of $Pb_5S_2I_6$ whiskers and tubules. *Inorg. Chem. Commun.* **6**, 270–274 (2003).
119. O.N. Yunakova, V.K. Miloslavskii, and E.N. Kovalenko: UV absorption spectra of thin films of Cs_2CdI_4 and Rb_2CdI_4 ferroelectrics. *Phys. Solid State* **45**, 888–892 (2003).
120. W. Hydaradjan and F. Voolless: UV-induced kinetics of second harmonic generation in CdI_2–Cu layered nanocrystals. *Opt. Commun.* **221**, 115–120 (2003).
121. H.W. Chen, N. Sakai, M. Ikegami, and T. Miyasaka: Emergence of hysteresis and transient ferroelectric response in organo-lead halide perovskite solar cells. *J. Phys. Chem.* **6**, 164–169 (2015).
122. H.Y. Ye, Y. Zhang, D.W. Fu, and R.G. Xiong: An above-room-temperature ferroelectric organo-metal halide perovskite: (3-pyrrolinium)($CdCl_3$). *Angew. Chem., Int. Ed. Engl.* **53**, 11242–11247 (2014).
123. A. Filippetti, P. Delugas, M.I. Saba, and A. Mattoni: Entropy-suppressed ferroelectricity in hybrid lead-iodide perovskites. *J. Phys. Chem.* **6**, 4909–4915 (2015).

124. Z.T. Jiang, B.D. James, J. Liesegang, K.L. Tan, R. Gopalakrishnan, and I. Novak: Investigation of the ferroelectric phase transition in $(CH_3NH_3)HgCl_3$. *J. Phys. Chem.* **56**, 277–283 (1995).
125. Y. Kutes, L. Ye, Y. Zhou, S. Pang, B.D. Huey, and N.P. Padture: Direct observation of ferroelectric domains in solution-processed $CH_3NH_3PbI_3$ perovskite thin films. *J. Phys. Chem.* **5**, 3335–3339 (2014).
126. S. Liu, F. Zheng, N.Z. Koocher, H. Takenaka, F. Wang, and A.M. Rappe: Ferroelectric domain wall induced band gap reduction and charge separation in organometal halide perovskites. *J. Phys. Chem.* **6**, 693–699 (2015).
127. G. Pilania and T. Lookman: Electronic structure and biaxial strain in $RbHgF_3$ perovskite and hybrid improper ferroelectricity in $(Na,Rb)Hg_2F_6$ and $(K,Rb)Hg_2F_6$ superlattices. *Phys. Rev. B* **90**, 115121 (2014).
128. G. Pilania and B.P. Uberuaga: Cation ordering and effect of biaxial strain in double perovskite $CsRbCaZnCl_6$. *J. Appl. Phys.* **117**, 114103 (2015).
129. M.I.B. Utama, M. de la Mata, C. Magen, J. Arbiol, and Q. Xiong: Twinning-, polytypism-, and polarity-induced morphological modulation in nonplanar nanostructures with van der Waals epitaxy. *Adv. Funct. Mater.* **23**, 1636–1646 (2013).
130. L.G. Schulz: Growth of alkali halide crystals from the vapor phase and from solution onto substrates of mica. *Acta Crystallogr.* **4**, 483–486 (1951).
131. J. Shigeta: Oriented overgrowth of evaporated crystallites fluoride crystallites on cleavage surfaces of single crystals. *J. Phys. Soc. Jpn.* **11**, 206–210 (1956).
132. L.J. Rabbitt, M.J. Hampshire, R.D. Tomlinson, and J.H. Calderwood: Low-frequency polarization in epitaxial NaCl thin films. In *Conference on Electrical Insulation & Dielectric Phenomena—Annual Report 1972*, G.S. Eager, Jr., ed. (IEEE, Washington D.C., 1972); pp. 359–367.
133. M. Kiguchi, S. Entani, K. Saiki, H. Inoue, and A. Koma: Two types of epitaxial orientations for the growth of alkali halide on fcc metal substrates. *Phys. Rev. B* **66**, 155424 (2002).
134. S. Fölsch, A. Helms, S. Zöphel, J. Repp, G. Meyer, and K.H. Rieder: Self-organized patterning of an insulator-on-metal system by surface faceting and selective growth: NaCl/Cu (211). *Phys. Rev. Lett.* **84**, 123 (2000).
135. S. Fölsch, A. Helms, and K.H. Rieder: Epitaxy of ionic insulators on a vicinal metal substrate: KCl and RbI on Cu (211). *Appl. Surf. Sci.* **162–163**, 270–274 (2000).
136. R. Bennewitz, V. Barwich, M. Bammerlin, C. Loppacher, M. Guggisberg, A. Baratoff, E. Meyer, and H.J. Güntherodt: Ultrathin films of NaCl on Cu (111): A LEED and dynamic force microscopy study. *Surf. Sci.* **438**, 289–296 (1999).
137. R. Bennewitz, A.S. Foster, L.N. Kantorovich, M. Bammerlin, C. Loppacher, S. Schär, M. Guggisberg, E. Meyer, and A.L. Shluger: Atomically resolved edges and kinks of NaCl islands on Cu (111): Experiment and theory. *Phys. Rev. B* **62**, 2074 (2000).
138. W. Hebenstreit, M. Schmid, J. Redinger, R. Podloucky, and P. Varga: Bulk terminated NaCl (111) on aluminum: A polar surface of an ionic crystal? *Phys. Rev. Lett.* **85**, 5376 (2000).
139. W. Hebenstreita, J. Redingerb, Z. Horozovaa, M. Schmida, R. Podlouckyc, and P. Vargaa: Atomic resolution by STM on ultra-thin films of alkali halides: Experiment and local density calculations. *Surf. Sci.* **424**, L321–L328 (1999).
140. D. Wolf: Reconstruction of NaCl surfaces from a dipolar solution to the Madelung problem. *Phys. Rev. Lett.* **68**, 3315 (1992).
141. J. Repp, S. Fölsch, G. Meyer, P. Drude, and K-H. Rieder: Ionic films on vicinal metal surfaces: Enhanced binding due to charge modulation. *Phys. Rev. Lett.* **86**, 252 (2001).
142. S. Fölsch, A. Helms, A. Riemann, J. Repp, G. Meyer, and K.H. Rieder: Nanoscale surface patterning by adsorbate-induced faceting and selective growth: NaCl on Cu (211). *Surf. Sci.* **497**, 113–126 (2002).
143. M. Kiguchi, K. Saiki, T. Sasaki, Y. Iwasawa, and A. Koma: Heteroepitaxial growth of LiCl on Cu (001). *Phys. Rev. B* **63**, 205418 (2001).
144. M. Kiguchi, H. Inoue, K. Saiki, T. Sasaki, Y. Iwasawa, and A. Koma: Electronic structure of alkali halide–metal interface: LiCl (001)/Cu (001). *Surf. Sci.* **522**, 84–89 (2003).
145. M.H. Yang and C.P. Flynn: Growth of alkali halides from molecular beams: Global growth characteristics. *Phys. Rev. Lett.* **62**, 2476–2479 (1989).
146. M.H. Yang and C.P. Flynn: Growth of alkali halides by molecular-beam epitaxy. *Phys. Rev. B* **41**, 8500–8508 (1990).
147. R. Klauser, M. Kubota, Y. Murata, M. Oshima, Y. Yamada Maruo, T. Kawamura, and T. Miyahara: Electronic properties of ionic insulators on semiconductor surfaces: Alkali fluorides on GaAs (100). *Phys. Rev. B* **40**, 3301–3305 (1989).
148. R. Klauser, M. Oshima, H. Sugahara, Y. Murata, and H. Kato: RbF as reactive and dipole interlayers between the Ge/GaAs interface. *Phys. Rev. B* **43**, 4879 (1991).
149. K. Saiki: Fabrication and characterization of epitaxial films of ionic materials. *Appl. Surf. Sci.* **113**, 9–17 (1997).
150. M. Kiguchi, K. Saiki, and A. Koma: Heteroepitaxial growth of alkali halide solid solution on GaAs (100). *J. Cryst. Growth* **237–239**(Part 1), 244–248 (2002).
151. M. Kiguchi, T. Yokoyama, T. Tsuduki, S. Terada, Y. Kitajima, and T. Ohta: Heteroepitaxial growth of KCl on a cleaved (001) face of KBr studied by extended X-ray-absorption fine structure. *Surf. Sci.* **433–435**, 595–599 (1999).
152. M. Kiguchi, K. Saiki, and A. Koma: Effects of anharmonicity of ionic bonds on the lattice distortion at the interface of alkali halide heterostructures. *Surf. Sci.* **470**, 81–88 (2000).
153. P. Chen, P.S. Kuttipillai, L. Wang, and R.R. Lunt: Homoepitaxial growth of metal halide crystals investigated by reflection high-energy electron diffraction. *Sci. Rep.* **7**, 40542 (2017).
154. G. Sáfrán, O. Geszti, G. Radnóczi, P.B. Barna, and K. Tóth: TEM study of the structure and morphology of AgI crystals formed on Ag (001), (011) and (111) thin films. *Thin Solid Films* **259**, 96–104 (1995).
155. G. Cochrane: Epitaxial growth of layers of hexagonal silver iodide. *J. Cryst. Growth* **7**, 109–112 (1970).
156. L.E. Brady, J.W. Castle, and J.F. Hamilton: Epitaxial silver halide films. *Appl. Phys. Lett.* **13**, 76–78 (1968).
157. L. Chen, W. Xie, G. Wang, I. Bhat, S. Zhang, A. Goyal, and T-M. Lu: Heteroepitaxy of large grain Ge film on cube-textured Ni (001) foils through CaF_2 buffer layer. *Thin Solid Films* **603**, 428–434 (2016).
158. Y.Y. Maruo, M. Oshima, T. Waho, and T. Kawamura: Photoemission and RHEED studies of bonding properties at the CaF_2/GaAs (001) interface. *Jpn. J. Appl. Phys.* **28**, L299 (1989).
159. M. Sugiyama and M. Oshima: MBE growth of fluorides. *Microelectron. J.* **27**, 361–382 (1996).
160. K.M. Colbow, T. Tiedje, D. Rogers, and W. Eberhardt: Photoemission study of the formation of the CaF_2/GaAs (100) interface. *Phys. Rev. B* **43**, 9672–9677 (1991).
161. T. Waho and H. Saeki: Electrical properties of $(CaSr)F_2$/GaAs (111)B interfaces grown by molecular beam epitaxy: Realization of unpinning. *Jpn. J. Appl. Phys.* **30**, 221–227 (1991).
162. M.A. Engelhardt, H. Höchst, K. Stair, J. Zajac, and F. Chambers: Photoemission study of $Ca_{1-x}Sr_xF_2$ films grown by MBE on GaAs (100). *Phys. Scr.* **41**, 896–900 (1990).
163. F. Santiago, T.K. Chu, and M.F. Stumborg: Process for forming epitaxial BaF_2 on GaAs. U.S. Patent US5435264 A, 1995.

164. W. Weiss, K. Kasper, K.H. Herrmann, D. Schmeisser, and W. Göpel: Surface morphology of epitaxial CaF_2 and SrF_2 layers grown onto InP (001) studied by atomic force microscopy and low-energy electron diffraction. *Surf. Sci.* **268**, 319–324 (1992).
165. N.S. Sokolov and S.M. Suturin: MBE growth of calcium and cadmium fluoride nanostructures on silicon. *Appl. Surf. Sci.* **175–176**, 619–628 (2001).
166. A.N. Tiwari, W. Floeder, S. Blunier, H. Zogg, and H. Weibel: Molecular beam epitaxial growth of (100) oriented CdTe on Si (100) using BaF_2–CaF_2 as a buffer. *Appl. Phys. Lett.* **57**, 1108–1110 (1990).
167. M. Bujor and R.W. Vook: Epitaxial poly- and monocrystalline CaF_2 films. *J. Appl. Phys.* **40**, 5373–5382 (1969).
168. W.M. Tong, E.J. Snyder, R. Stanley Williams, A. Yanase, Y. Segawa, and M.S. Anderson: Atomic force microscope studies of CuCl island formation on CaF_2 (111) substrates. *Surf. Sci. Lett.* **277**, L63–L69 (1992).
169. W. Chen, M. Dumas, S. Ahsan, A. Kahn, C.B. Duke, and A. Paton: Epitaxial growth and characterization of CuCl (110)/GaP (110). *J. Vac. Sci. Technol., A* **10**, 2071–2076 (1992).
170. T. Wake, K. Saiki, and A. Koma: Epitaxial growth and surface structure of cuprous halide thin films. *J. Vac. Sci. Technol., A* **18**, 536–542 (2000).
171. A. Yanase and Y. Segawa: Nucleation and morphology evolution in the epitaxial growth of CuCl on MgO (001) and CaF_2 (111). *Surf. Sci.* **357**, 885–890 (1996).
172. A. Yanase and Y. Segawa: Two different in-plane orientations in the growths of cuprous halides on MgO (001). *Surf. Sci.* **329**, 219–226 (1995).
173. A. Yanase and Y. Segawa: Stranski-krastanov growth of CuCl on MgO (001). *Surf. Sci.* **367**, L1–L7 (1996).
174. A. Yanase, Y. Segawa, M. Mihara, W.M. Tong, and R.S. Williams: Heteroepitaxial growth of CuCl on MgO (001) substrates. *Surf. Sci.* **278**, L105–L109 (1992).
175. M. Wu, Q. Guo, and P.J. Møller: Ultrathin films of CuCl on TiO_2 (110): Electronic structure and surface reconstruction. *Vacuum* **41**, 1418–1421 (1990).
176. R. Ai, X. Guan, J. Li, K. Yao, P. Chen, Z. Zhang, X. Duan, and X. Duan: Growth of single-crystalline cadmium iodide nanoplates, CdI_2/MoS_2 (WS_2, WSe_2) van der Waals heterostructures, and patterned arrays. *ACS Nano* **11**, 3413–3419 (2017).
177. H. Bengel, H.J. Cantow, S.N. Magonov, H. Hillebrecht, G. Thiele, W. Liang, and M.H. Whangbo: Tip-force induced surface corrugation in layered transition metal trichlorides MCl_3 (M = Ru, Mo, Rh, Ir). *Surf. Sci.* **343**, 95–103 (1995).
178. S.T. Ha, X.F. Liu, Q. Zhang, D. Giovanni, T.C. Sum, and Q.H. Xiong: Synthesis of organic–inorganic lead halide perovskite nanoplatelets: Towards high-performance perovskite solar cells and optoelectronic devices. *Adv. Opt. Mater.* **2**, 838–844 (2014).
179. Y. Nagamune, S. Takeyama, N. Miura, T. Minagawa, and A. Misu: Very thin PbI_2 single crystals grown by a hot wall technique. *Appl. Phys. Lett.* **50**, 1337–1339 (1987).
180. T. Ueno, H. Yamamoto, K. Saiki, and A. Koma: Van der Waals epitaxy of metal dihalide. *Appl. Surf. Sci.* **113**, 33–37 (1997).
181. H. Kurisu, S. Yamamoto, O. Sueoka, and M. Matsuura: Preparation and quantum confinement effect of PbI_2CdI_2 superlattices. *Solid State Commun.* **99**, 541–545 (1996).
182. Y. Wang, Y-Y. Sun, S. Zhang, T-M. Lu, and J. Shi: Band gap engineering of a soft inorganic compound PbI_2 by incommensurate van der Waals epitaxy. *Appl. Phys. Lett.* **108**, 013105 (2016).
183. S. Takeyama, K. Watanabe, M. Ichihara, K. Suzuki, and N. Miura: Van der Waals epitaxial growth of thin BiI_3 films on PbI_2 and CdI_2 substrates by a hot wall method. *J. Appl. Phys.* **68**, 2735–2738 (1990).
184. A. Mowbray and R.G. Jones: Homo- and hetero-iodide thin film growth on InSb (001): Low-temperature iodide formation and epitaxial growth of CdI_2. *Appl. Surf. Sci.* **48**, 27–38 (1991).
185. T. Suzuki and R. Souda: Structure analysis of CsCl deposited on the MgO (001) surface by coaxial impact collision atom scattering spectroscopy (CAICASS). *Surf. Sci.* **442**, 283–290 (1999).
186. G. Yoshikawa, M. Kiguchi, K. Ueno, A. Koma, and K. Saiki: Visible light photoemission and negative electron affinity of single-crystalline CsCl thin films. *Surf. Sci.* **544**, 220–226 (2003).
187. M. Kiguchi, S. Entani, K. Saiki, and A. Koma: Atomic and electronic structure of CsBr film grown on LiF and KBr (001). *Surf. Sci.* **523**, 73–79 (2003).
188. Y. Wang, Y. Shi, G. Xin, J. Lian, and J. Shi: Two-dimensional van der Waals epitaxy kinetics in a three-dimensional perovskite halide. *Cryst. Growth Des.* **15**, 4741–4749 (2015).
189. Q. Zhang, R. Su, X. Liu, J. Xing, T.C. Sum, and Q. Xiong: High-quality whispering-gallery-mode lasing from cesium lead halide perovskite nanoplatelets. *Adv. Funct. Mater.* **26**, 6238–6245 (2016).
190. Y. Wang, X. Sun, R. Shivanna, Y. Yang, Z. Chen, Y. Guo, G-C. Wang, E. Wertz, F. Deschler, Z. Cai, H. Zhou, T-M. Lu, and J. Shi: Photon transport in one-dimensional incommensurately epitaxial $CsPbX_3$ arrays. *Nano Lett.* **16**, 7974–7981 (2016).
191. J. Chen, Y. Fu, L. Samad, L. Dang, Y. Zhao, S. Shen, L. Guo, and S. Jin: Vapor-phase epitaxial growth of aligned nanowire networks of cesium lead halide perovskites ($CsPbX_3$, X = Cl, Br, I). *Nano Lett.* **17**, 460–466 (2017).
192. Y. Wang, Z. Chen, F. Deschler, X. Sun, T-M. Lu, E.A. Wertz, J-M. Hu, and J. Shi: Epitaxial halide perovskite lateral double heterostructure. *ACS Nano* **11**, 3355–3364 (2017).
193. L. Niu, X. Liu, C. Cong, C. Wu, D. Wu, T.R. Chang, H. Wang, Q. Zeng, J. Zhou, X. Wang, W. Fu, P. Yu, Q. Fu, S. Najmaei, Z. Zhang, B.I. Yakobson, B.K. Tay, W. Zhou, H.T. Jeng, H. Lin, T.C. Sum, C. Jin, H. He, T. Yu, and Z. Liu: Controlled synthesis of organic/inorganic van der Waals solid for tunable light-matter interactions. *Adv. Mater.* **27**, 7800–7808 (2015).
194. S-T. Ha, C. Shen, J. Zhang, and Q. Xiong: Laser cooling of organic–inorganic lead halide perovskites. *Nat. Photonics* **10**, 115–121 (2016).
195. J. Liu, Y. Xue, Z. Wang, Z-Q. Xu, C. Zheng, B. Weber, J. Song, Y. Wang, Y. Lu, Y. Zhang, and Q. Bao: Two-dimensional $CH_3NH_3PbI_3$ perovskite: Synthesis and optoelectronic application. *ACS Nano* **10**, 3536–3542 (2016).
196. R.F.C. Farrow, S.S.P. Parkin, and K.P. Roche: Epitaxial growth of rare earths on rare earth fluorides and rare earth fluorides on rare earths: Two new epitaxial systems accessed by MBE. *MRS Proc.* **103**, 205–210 (1987).
197. R.F.C. Farrow, S.S.P. Parkin, V.S. Speriosu, A. Bezinge, and A.P. Segmuller: Structural and magnetic characterization of rare earth and transition metal films grown on epitaxial buffer films on semiconductor. *MRS Proc.* **151**, 203–211 (1989).
198. R.F.C. Farrow, M.F. Toney, B.D. Hermsmeier, S.S.P. Parkin, and D.G. Wiesler: Synchrotron X-ray diffraction studies of the lattice and magnetic structure of epitaxial Dy films in LaF_3/Dy/LaF_3 sandwiches. *J. Appl. Phys.* **70**, 4465–4468 (1991).